Summer 2022

Ultrasonic NDT Methods for the Evaluation of Post-Tensioned Systems with Flexible Fillers

Denis McDonald
Embry-Riddle Aeronautical University, mcdond12@my.erau.edu

Scholarly Commons Citation

McDonald, Denis, "Ultrasonic NDT Methods for the Evaluation of Post-Tensioned Systems with Flexible Fillers" (2022). *Doctoral Dissertations and Master's Theses*. 674.
https://commons.erau.edu/edt/674

ULTRASONIC NDT METHODS FOR THE EVALUATION OF POST-TENSIONED SYSTEMS WITH FLEXIBLE FILLERS

by

Denis McDonald

Thesis Submitted to the College of Engineering Department of Civil Engineering in Partial Fulfillment of the Requirements for the Degree of

Master of Science in Civil Engineering

August 2022

Embry-Riddle Aeronautical University

Daytona Beach, Florida

Acknowledgments

I am honored to have had the opportunity to carry out this research, which could not have been accomplished without the support provided to me by Embry-Riddle Aeronautical University. I would first like to thank my advisor Dr. Jeff Brown, Professor and Program Coordinator for M.S. and B.S. in Civil Engineering. Without him, I would never have been able to undertake this fantastic opportunity to explore this research, nor would I have been able to pursue a master’s degree in Civil Engineering. His constant guidance and expertise provided me with everything I needed to succeed in pursuing this degree.

Additionally, I would like to acknowledge the Embry-Riddle Civil Engineering program and its faculty. Without their support and knowledge, I could never have hoped to achieve my academic goals.

I would also like to thank the Florida Department of Transportation, who funded this research project, and the Federal Highway Administration - Dwight D. Eisenhower Fellowship program, which assisted in funding my master’s degree.

Finally, thank you to my friends, partner, and family for all the support you have provided me throughout my schooling. I especially would like to thank my late Father and Grandmother, whose support and advice encouraged me to continue my degree even in the most challenging times.

Abstract

Researcher: Denis McDonald
Title: Ultrasonic NDT Methods for the Evaluation of Post-Tensioned Systems with Flexible Fillers
Institution: Embry-Riddle Aeronautical University
Degree: Master of Science in Civil Engineering
Year: 2022

Non-destructive evaluation of post-tensioned structures with flexible fillers is desperately needed due to their rapid implementation in the State of Florida, primarily in roadway structures. This study provides an overview of existing evaluation methods for traditional post-tensioned structures with cementitious grouts and further explores two promising methods to be applied to flexible filler systems. The first method, diffuse ultrasound spectroscopy, indirectly evaluates post-tensioned structures by quantifying the severity of microcracking in the structure. Microcrack detection is accomplished by processing received waveforms generated with a pitch-catch transducer configuration. The second method, coda-wave interferometry, measures the velocity variation at the tail end of waveforms, known as the coda, between varying stress states of a structure. The velocity variation can be correlated to cracking events, structural yielding, and stress level changes. First, preliminary testing was done for both methods to find the optimal test setup and validate the methods' efficacy. Algorithms were developed for both promising methods using the preliminary testing data for development. Next, the methods underwent experimental testing composed of direct compression and 3-point load testing on normally reinforced and post-tensioned small-scale beams. The experiments show the methods' effectiveness in indirectly evaluating the health of the post-tensioning system with flexible fillers. Overall, the two methods prove to be very promising and are recommended to be explored in further studies.

Table of Contents

List of Figures

List of Tables

List of Equations

Nomenclature

CG – cementitious grout
CWI – Coda-Wave Interferometry
DU – Diffuse Ultrasound
FDOT - Florida Department of Transportation
FF– flexible filler
NDE – non-destructive evaluation
PT- post-tensioned

Chapter I: Introduction

1.1. Statement of the Problem

This research focuses on identifying a solution for evaluating post-tensioned (PT) systems with flexible fillers in transportation applications. Typical applications include tendons in segmental bridges, PT I-beams, hammerhead piers, straddle–bent piers, and C-piers. This evaluation method must be non-destructive and provide insight into the condition of the PT system, which tends to be damaged by external forces such as water ingress. When combined with voids in the filler material, these external conditions can cause rapid corrosion of the PT tendon and, therefore, must be detected early to avoid costly structural repairs. Despite decades of research, the FDOT still lacks a reliable method outside visual inspections to perform NDE on CG or FF post-tensioning systems.

1.2. Applications of Flexible Fillers

After several events of deficient performance with cementitious grout systems, the FDOT provided guidance regarding the use of flexible fillers in the 2016 Structural Design Guidelines (FDOT, 2016). The permitted applications are as follows:

1. External tendons
2. Tendons with vertical deviation greater than 20'
3. Tendons in I-beams
4. Tendons in U-Girders
5. Strand tendons with predominantly vertical geometry
6. Continuity tendons in segmental box girders

Later, the FDOT modified a list of exceptions where flexible fillers could not be used (FDOT, 2021). These changes affirm the use of flexible filler PT systems in Florida's future PT transportation structures. The list of exceptions includes:

1. Top slab cantilever longitudinal tendons in segmental box girders
2. Top slab transverse tendons in segmental box girders
3. Tendons that are draped 2' or less in post-tensioned slab-type superstructures

The FDOT provided further information on why these exceptions still exist, mainly citing the lack of structural rigidity provided by the flexible fillers and the proximity to the roadway of the outlined conditions (FDOT, 2021).

1.3. Objectives

This research aims to identify promising non-destructive evaluation methods for use on flexible filler post-tensioned systems throughout Florida. This objective will be split into five secondary goals.

1. Perform background research into NDE methods used on traditional grouted PT systems, which may translate well into use on flexible fillers, and isolate one or two promising techniques for scale testing.
2. Perform preliminary testing to identify hardware, set up procedures, and access the needs of the algorithms used to analyze the data collected.
3. Develop the algorithms to analyze the data gathered from preliminary testing for use in small-scale beam testing.

4. Perform small-scale testing of the chosen methods using two scale beams and analyze the data gathered from these experiments.
5. Using the data gathered, provide recommendations for the further implementation of these methods, or describe alternative options for future flexible filler NDE.

1.4 Methodology

The first step in this process will be to gather information from previous studies and then choose the two most promising methods for the applications of flexible fillers. From there, a knowledge base is collected on how to carry out experiments, including the equipment needed, sensor development or placement, and the development of any necessary algorithms. Small-scale testing will then be carried out, first on a small reinforced concrete block undergoing direct compression, then on small-scale reinforced beams, one being a traditionally reinforced and the other a post-tensioned beam. These beams will be tested via three-point loading until cracking.

Chapter 2: Relevant Literature

2.1. Non-Destructive Testing used on Cementitious Grouts

Though there has been little research into the in-service inspection of PT systems with flexible fillers, there is an extensive body of knowledge regarding the inspection of traditional grouted PT specimens. This work will focus on identifying corrosion on the steel strands and finding areas in which the grout does not protect the strands, such as deterioration or voids in the grout. As both phenomena are likely to occur in FF tendons, these research papers are a solid foundation for inspecting FF systems. Listed in the following subsections will be some of the most used methods of identifying issues with CG systems.

2.1.1 Magnetic Flux Leakage

Magnetic flux leakage (MFL) relies on the interaction between ferrous materials and magnetic fields. Magnetic flux leakage applies this interaction to find stresses in ferrous materials such as steel, which can be caused by either cross-sectional loss in reinforcement strands or oxidation of strands. The MFL method relies on magnetically saturating the strands. When areas with section loss or corrosion are saturated, the magnetic flux is forced to flow through the air as it becomes the least resistant path (Azizinanmini, 2012). This leakage can be quantified by measuring the vertical component of the magnetic field flowing through the air with a Hall Effect sensor. These inspection methods have been used repetitively in many industrial fields, such as nuclear power, cable-stay bridges, segmental box beam bridges, PT bridges, natural gas, and oil pipelines. With the successful implementation of non-destructive inspection in these fields, it is expected that applying these methods to PT bridges with flexible fillers will be fruitful.

A study performed by Hurlebaus utilizing this method implemented a commercial device by NDT Technologies Inc. to test the feasibility of this approach on external PT ducts (Figure 1). The device was moved along the duct to identify these using prepared samples for multiple types of tendons and duct defects. The data from this device is then sent to a portable unit for data analysis. The results from this study test for MFL were encouraging for metal and HDPE ducts. The metric used for research, in this case, was LMA or loss of metallic area. The results from this study indicate a strong success rate in identifying metallic faults in PT ducts (Hurlebaus, Hueste, Karthik, & Terzioglu, 2016).

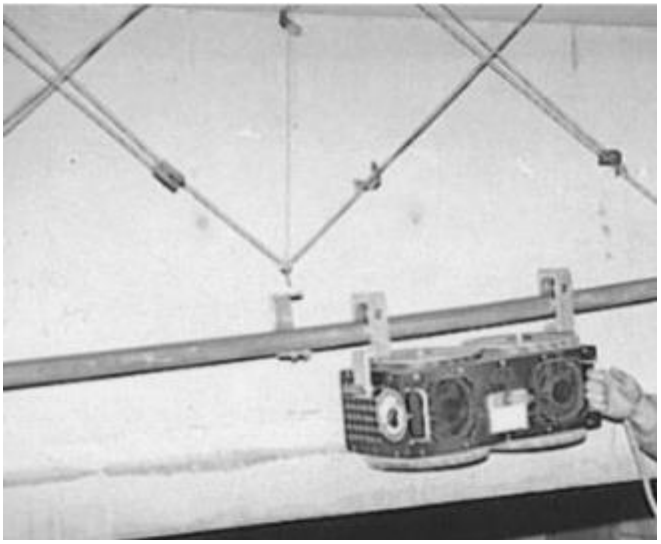

Figure 1 MFL Device for the detection of grout voids and strand defects (Hurlebaus, Hueste, Karthik, & Terzioglu, 2016)

2.1.2. Magnetic Flux Method – Permanent Magnet

Active methods for MFL inspection involve using a mobile device consisting of two permanent or electric magnets, along with hall-effect sensors to find areas of corrosion or cross-section loss in steel tendons. As this device is moved along the length of the tendon, it saturates the steel between the two magnets, which induces a magnetic field within the tendon. If the tendon being inspected has regions of corrosion or section loss, the device will identify magnetic field leakages from the tendon as it moves atop them.

Such a device was designed and prototyped for the Virginia Transportation Research Council (VTRC) for use on prestressed concrete box bridges.

Active MFL methods show promise in situations where large sections of corrosion or area loss may be present in a tendon because active methods are unable to detect minor defects. However, they are portable, cheap, and easily used by inspection crews. These small devices are to be run along the surface of the PT duct and can detect tendon loss at an approximate resolution of 0.1 inches with 2 inches of cementitious cover (Chase, 2020). In this study, section loss was detected by comparing the flux densities in the x and y planes as read by the Hall Effect sensors. As the variation between the two density plots increases, it can be inferred that the section loss is also growing at a relative rate (Chase, 2020). This result can also be seen from laboratory results from the same study where their data correlates with the prepared tendon samples.

A similar unit as the one produced for the VTRC was used in a study by the University of Toledo to inspect operational prestressed box bridges. Using their sensor, the UT could find a linear relationship between the magnetic flux readings from their Hall Effect sensor and the level of deterioration of the steel strands in question (Fernandes & Nims, 2014). These findings were then confirmed on other operating bridges in Ohio. Using the results from the experiments, it is possible to accurately find and diagnose sections of steel strands with deterioration. However, success has been had with inspecting strands with minimal to no other mild reinforcing steel, which is not a practical inspection case regarding internal PT ducts.

A study performed by Nanjing University of Aeronautics and Astronautics found a solution to minimize the effects of interfering ferrous materials during an MFL inspection.

This solution is a signal processing method that utilizes the moving average method. This method operates by averaging several points from the input signal to produce each point in the output signal (Xu, Wang, & Wu, 2012). In simpler terms, this method averages the data points collected from a high sample rate sensor to remove MFL variations caused by mild reinforcing steel that may get in the way of internal PT ducts. The differences between the original and filtered results where the peaks in the filtered results correlate to the areas of section loss in the measured strand, which can be easily seen from the program output.

2.1.3. Magnetic Flux Method – Solenoid

This process utilizes a coil of wire set around the tendon in question, and an external source magnetizes the tendon to gather readings on the condition of the tendon. The coil of wire can be run along the duct length if there is no obstruction. This method can find defects in the tendon, such as corrosion or section loss (Hurlebaus, Hueste, Karthik, & Terzioglu, 2016). The main advantage of this method is the accuracy at which the coil device can locate the point of interest. Testing was performed on multiple prepared specimens with varying degrees of section loss, breakage, or voids in the tendon or PT duct. This method can detect defects in the tendon at a minimum of 0.2% cross-sectional loss (Hurlebaus, Hueste, Karthik, & Terzioglu, 2016). Testing also proved what was expected; with regards to this method being unable to detect voids of the grout material, it should also be noted that metal ducts significantly hindered this method. Overall, this method was very effective in identifying tendons that had no damage and could often detect areas of loss in the tendon. This study's data indicates a strong solenoid-type MFL NDE performance in identifying section loss, corrosion, and breakage of tendons within HDPE ducts. It is also able to locate tendons that are in good condition. The main drawback of this method is the amount of time needed for wrapping the cable around the duct and the complete access required to perform the testing, and its limited use on only external PT tendons.

2.1.4. Sonic/ Ultrasonic Pulse Velocity

The pulse velocity method relies on sending either sonic or ultrasonic waves through the material and comparing the calculated time of travel against the recorded time of travel for the waves through the material (Hurlebaus, Hueste, Karthik, & Terzioglu, 2016). This data can then be used to interpret what type of material defects occurred for the wave's travel time to change. Hurlebaus tested this method on internal ducts of both HDPE and metal construction. This testing used SPV and UPV sensors on opposing ends of the concrete surrounding the ducts. The wave was then sent and received by the sensors. Though SPV and UPV methods are proven, no conclusive data was able to be gathered due to the minor nature of the defects of interest compared to the distance the wave travels. Therefore, it is somewhat inconclusive with respect to the usability of the method.

2.1.5. Electrochemical Impedance Spectroscopy

Electrochemical Impedance Spectroscopy (EIS) relies on passing a low amplitude voltage through the steel in varying frequencies. The impedance of the cementitious filler can be found by measuring the signal amplitude and phase shift. In the Hurlebaus study, four holes were drilled into the HDPE pipe of the prepared external tendons for electrodes to be placed. These holes would later be filled with an HDPE welding substance. A portable power source powers the electrodes, and the electrodes are fed to a potentiostat. The readings from the potentiostat are then processed using a notebook computer to discover flaws in the tendon (Hurlebaus, Hueste, Karthik, & Terzioglu, 2016). This method was successful in positively identifying the broken and corroded strands within the prepared tendon. While relatively cost-effective, this method is somewhat invasive are it requires drilling into the HDPE duct. Also, this method is limited to external PT ducts.

2.2. Promising Methods

These methods are the most promising method for NDE of flexible fillers found during the literature review for this paper. They were selected for their effectiveness, ease of use, and accessibility, along with a vast body of information already available for these methods.

2.2.1. Diffuse Ultrasound

Diffuse ultrasound is an adaptation of traditional ultrasonic pulse-echo (UPE) methods, which usually operate below the threshold of 50kHz. The limit on traditional UPE is motivated by the reduction of wave scattering within the material; this is especially true for non-homogeneous materials such as concrete, which is an amalgamation of sand, rocks, cement, and sometimes other admixtures. If higher frequency waves are used with UPE on concrete structures, say at or above 50kHz, the waves will scatter on the distinct aggregates and binder material, making the received signal noisy and challenging to analyze for useful information.

Diffuse ultrasound takes advantage of this scattering by closely looking at the properties of the end or coda of the returned waveform. Since DU relies on the scattering of the induced wave, high-frequency transducers are employed to maximize scattering. The focus of the literature review on this method is the application of DU to find microcracking of concrete, which would indicate a loss of PT force, allowing for an increase of tension in the PT structure.

One of the earliest studies of DU in concrete structures was performed by Anugonda in the early 2000s. This study identified that peak ultrasonic diffusivity and dissipation range could be centered on a frequency of 500kHz (Anugonda, Wiehn, & Turner, 2001). The diffusivity of a material is a measured quantity indicative of the microstructure of the material. At the same time, dissipation will characterize the viscoelastic properties of the material; both quantities will be subject to change as there is an increase of damage to the structure (Anugonda, Wiehn, & Turner, 2001). As high-frequency waves are being used, the wavelength is on a scale comparable to the individual aspects of the concrete material; this, in turn, allows for attenuation of the wave via dissipative mechanisms. As this attenuation occurs, the response of the material, concrete, in this case, becomes a combination of coherent and incoherent (diffuse) energy. The attenuation allows the returned waveform to be characterized by the following diffuse waveform equation in Equation 1, as outlined in the paper (Anugonda, Wiehn, & Turner, 2001).

$$\langle E(z,t)\rangle = E_0 \frac{1}{2\sqrt{\pi D t}} \mathrm{e}^{-z^2/4Dt} \mathrm{e}^{-\sigma t}.$$

Equation 1 Diffuse waveform equation (Anugonda, Wiehn, & Turner, 2001)

In this equation, diffusivity is represented by D, dissipation is represented by σ, and E0 is the initial energy. Using a non-linear regression fit, the data received by the receiving transducer can fit the equation. This fitting procedure will result in values for the three parameters: D, σ, and E_0, which will allow for the characterization of the material and damages to said material (Anugonda, Wiehn, & Turner, 2001). According to this paper, an increase of microcracking in the concrete due to damage (Figure 2), such as loss of PT force, would be flagged via a decrease in the diffusivity (D) because the wave will have a longer propagation path, therefore, decreasing the value of D.

Based on the same principles as the Anugonda research, a study by Quiviger proposed using two identical 500kHz transducers in a pitch-catch configuration to identify micro-cracking in samples with simulating cracking. These experiments were performed with notched concrete specimens to test DU's sensitivity to size variations of cracks. The two 500 kHz transducers were placed on a planar surface with the emitter a series of pulses and the receiver recording and then averaging the series of pulses to assist in noise reduction of the signal (Quiviger, Payan, Chaix, Garnier, & Salin, 2011). The processing of the averaged waveform followed the same steps as the Anugonda study, resulting in the same trends where the diffusivity value decreased proportionally to the size of the notch in the samples. This study concluded that DU could differentiate between different damage severity levels with excellent reliability (Quiviger, Payan, Chaix, Garnier, & Salin, 2011).

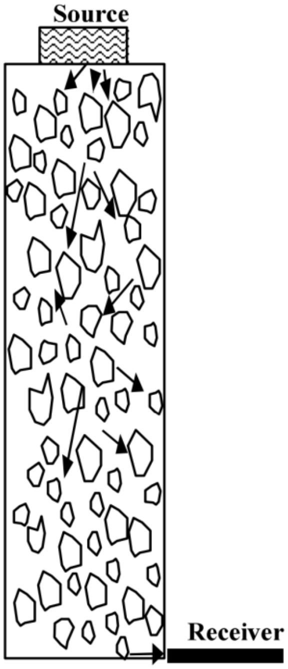

Figure 2 Experimental Setup showing how waves scatter in concrete between source and receiver (Anugonda, Wiehn, & Turner, 2001)

Another study using diffuse ultrasound for concrete focused on the analysis of prepared specimens by simulating microcracking using glass fibers at differing percentages. This study focused on the effectiveness of different received frequency bands at identifying the advent of microcracking in samples. The setup for this study is like the Quiviger study, using two 500kHz transducers in a pitch-catch configuration. The emitting transducer in this setup was pulsed 500 times, then received by the paired transducer, and averaged for signal clarity (Ahn, Myoungsu, Popovics, & Weaver, 2019). The input and output signals were amplified in this setup to assist with the activation of the transducer and the processing of the received signal. As for processing, Ahn used a modified version of the diffuse waveform equation to fit the testing setup better. The equation used can be seen in Equation 1Equation 2.

$$\log\langle E(x,y,z,t)\rangle = C_0 - \frac{3}{2}\log(Dt) - \frac{d^2}{4Dt} - \sigma t$$

Equation 2 Diffuse waveform equation by Ahn for curve fitting analysis (Ahn, Myoungsu, Popovics, & Weaver, 2019)

One of the significant differences in this equation is the use of $C_{0,}$ which is a constant related to the initial energy of the wave, with D and σ being the same. Aside from the varied waveform equation for the curve fitting Ahn, a similar processing approach as both Anugonda and Quiviger, this process can be seen in Figure 3.

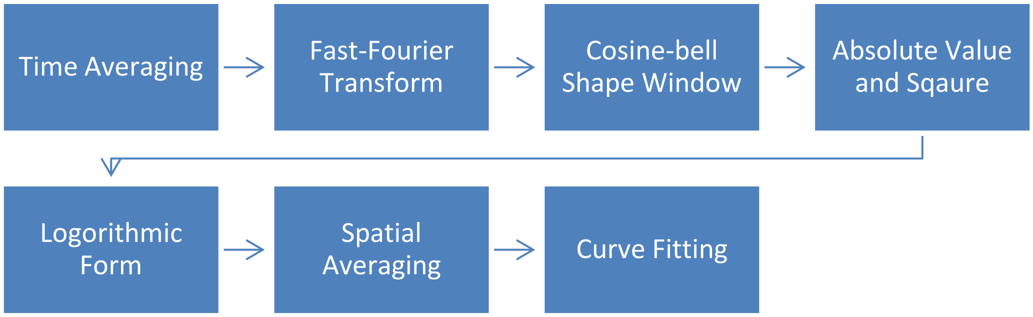

Figure 3 Algorithm process used by Ahn for finding the values of dissipation and diffusion (Ahn, Myoungsu, Popovics, & Weaver, 2019)

The reasoning behind the non-standard use of the cosine bell curve is to separate the received waveform into window sections centered around 200, 300, and 400 kHz. These individual components were compared and found to have varying energy densities. It was found that though the energy densities of these components varied, the trend of decreasing diffusivity with an increase in microcracking continued as expected (Ahn, Myoungsu, Popovics, & Weaver, 2019). Ahn used the windowed diffusivity results to calculate an average value for the diffusivity. A trend for the dissipation coefficient being as the simulated damage increases, the value of the dissipation coefficient would increase proportionally (Ahn, Myoungsu, Popovics, & Weaver, 2019). This study shows that diffuse ultrasound can detect slight changes in microcracking along with trends of both dissipation and diffusivity coefficients via curve-fitting and other processing without regard for the distance between transducers (Figure 4).

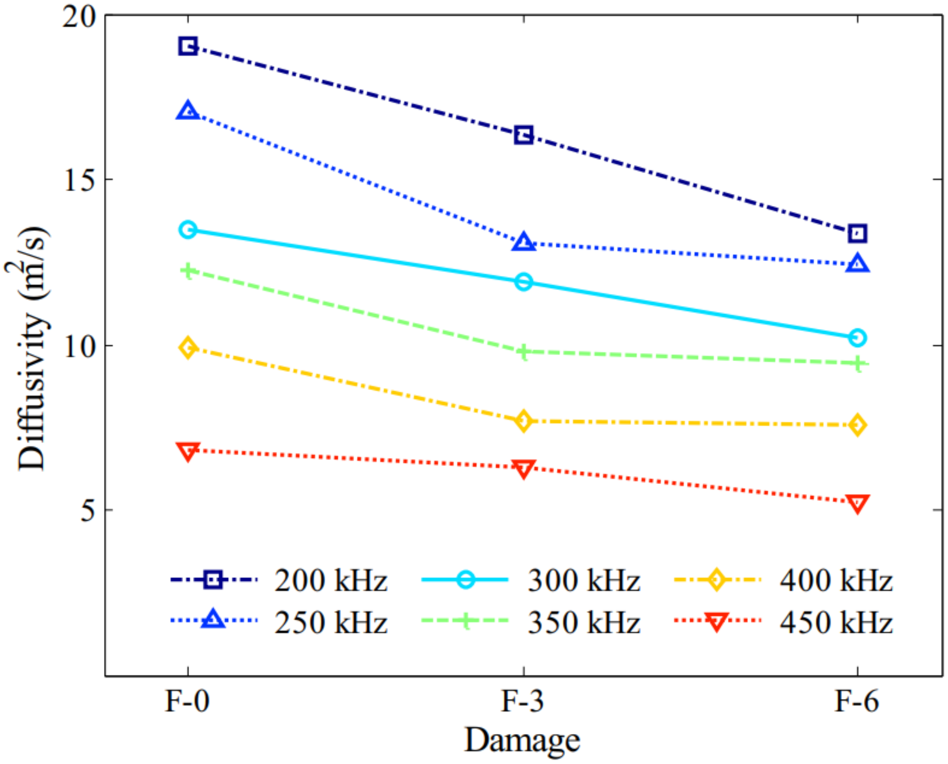

Figure 4 Results from Ahn's study show a decrease in diffusivity with respect to an increase in damage (Ahn, Myoungsu, Popovics, & Weaver, 2019)

2.2.3. Coda-wave Interferometry

A study by Anugonda speaks of how the analysis of scattered waves in a non-homogenous material such as concrete can show both the state of the concrete’s microstructure and the material's stress level (Anugonda, Wiehn, & Turner, 2001). CWI focuses on analyzing the returned waveform for time shifts between different stress levels, meaning that the velocity of the scattering wave through the concrete will be a function of stress level.

In a study by Larose, the effect of weak stress level changes on the coda-wave is measured. The measurement was accomplished by pulsing a transducer and measuring the coda of the wave returned to another transducer. According to Larose, as the stress level within the concrete increases, there will be a positive shift of the coda wave due to the velocity change of the wave as material stress increases (Larose & Hall, 2009). An example of the coda of a wave is shown in Figure 5.

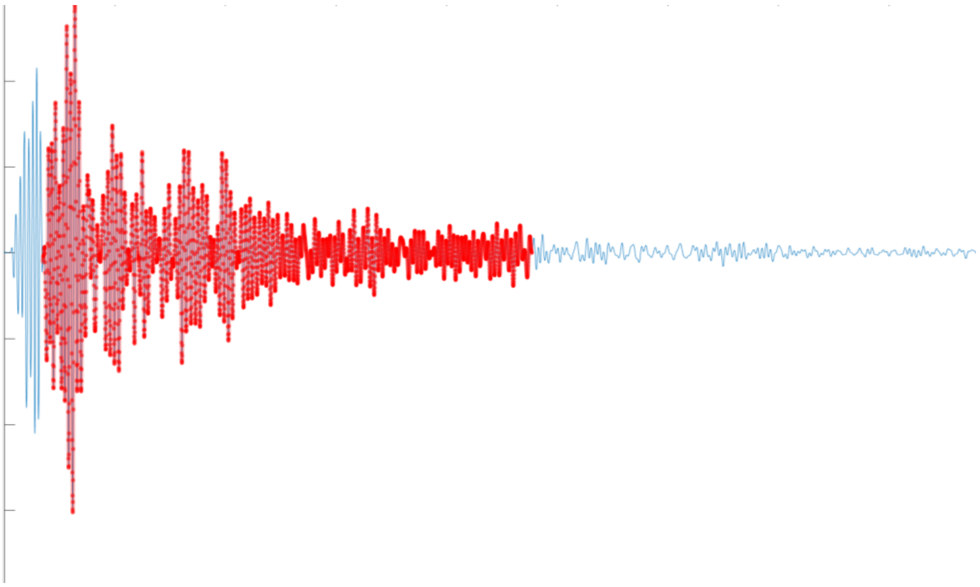

Figure 5 Coda-wave example waveform

The red portion of the waveform shown in Figure 5 is considered the coda-wave, which is the portion of the wave that arrives after the initial pulse is received. The coda wave can be identified as the waveform portion after the first major trough. The shift of the coda wave compared to waveforms taken at differing stress levels can be expressed as a velocity variation of the waveform. This velocity variation will increase when there is a shift in the stress experienced by the structure from which readings are collected (Larose, et al., 2006).

A study by Stähler provides a practical application-based approach to CWI on a concrete bridge. The study focuses on the construction of a concrete bridge and the identification of small velocity changes induced by changing stress states in the structure (Stahler & Sens-Schonfelder, 2011). Using a cross-correlation formula (Equation 3) to compare the initial conditions to further tests, Stähler was able to identify the time lag of the coda-wave.

$$CC^{\mathrm{S}}_{t_\kappa}(\varepsilon) = \frac{\int_{t_\kappa - T/2}^{t_\kappa + T/2} h'[t(1-\varepsilon)]h[t]dt}{\sqrt{\int_{t_\kappa - T/2}^{t_\kappa + T/2} h'^2[t(1-\varepsilon)]dt \int_{t_\kappa - T/2}^{t_\kappa + T/2} h^2[t]dt}}$$

Equation 3 Cross-correlation formula for CWI

Stähler performed direct compression experiments on a non-reinforced concrete block with pitch-catch transducers for measurements. During stressing in the initial test of the study, an almost linear stress-velocity relationship was seen. During the second loading, an increase in the velocity-stress relationship was experienced, which can be explained by the formation of cracking within the sample (Stahler & Sens-Schonfelder, 2011).

In a study by Zhang, an application of CWI with a direct tensile test was explored, where linear stress-velocity changes were expected in the opposite slope of direct compression testing. The velocity changes were shown clearly in the direct tensile testing, along with important information about the behavior of CWI in relation to previous maximum applied forces. The first behavior is the range in which the concrete has already experienced that loading level where the velocity decrease is based solely on the acoustoelastic effect due to no new microcrack formation (Zhang, et al., 2012). The second behavior is when the load is increased past its previous maximum and is affected by both the acoustoelastic effect and the effects of microcracking. In the study by Planès, this effect is spoken of in more detail, called the Kaiser effect, being a memory effect observed in concrete where additional microcracking will occur when the applied stress overtops the historical maximum (Planes & Larose, 2013).

Zhang utilized the same cross-correlation method to identify the time lag of the waveforms as Stähler with the same level of success. Under the level of tensile stress exerted in these experiments, the propagation velocity decreased by as much as 0.248% through both the influence of microcracking and the acoustoelastic effect. This study found that monitoring a concrete specimen’s damage level can be achieved by analyzing the effective acoustoelastic coefficient, which is found using the time lag value via cross-correlation of waveforms at varying stress levels.

An advantage of this method is its ability to identify stress level changes due to temperature fluctuations which cannot be analyzed using standard deformation-based sensors, such as strain gauges (Planes & Larose, 2013). A significant challenge of most displacement-based methods such as this will be the need for an initial measurement for use as a reference value. However, comparison along multiple locations on a prestressed structure could show differences in sections with proper and degraded levels of post-tensioning force.

Chapter 3: Test Setup

The setups for the diffuse ultrasound and coda-wave interferometry testing are very similar in terms of the equipment used. The equipment used for data collection, as well as the corresponding settings for the equipment, will be discussed in detail in this section. Multiple tests were completed to investigate different bonding methods for the transducers. The porous nature of concrete made it difficult to mechanically couple the two sets of transducers. The bonding issues will be explored in the transducer bonding section of this chapter.

The foundation for both algorithms was taken from the Anugonda, Ahn, and Planès papers. Each required specific adjustments for either diffuse ultrasound analysis or coda wave interferometry. This process will be outlined in detail in the algorithm section of this chapter.

3.1. Data Collection Equipment

The basis for the testing setups was mainly derived from the testing plan outlined in the Ahn study. Modifications included an additional set of transducers for coda-wave interferometry and varied amplification for both pre- and post-amplifications for the emitting and receiving transducers for each test type. A flow chart (Figure 6) and a list of the individual equipment pieces will follow in the list below:

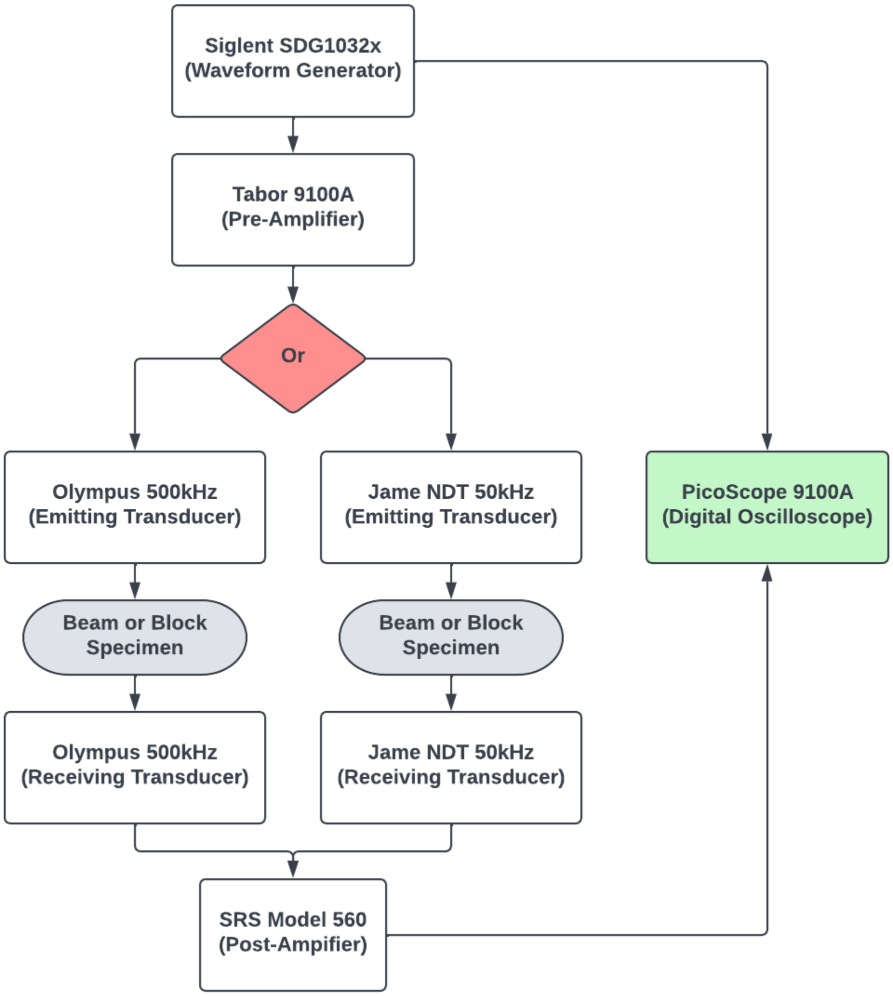

Figure 6 Experimental test equipment flowchart

3.1.1 Waveform Generator – Siglent SDG1032x

This waveform generator was chosen due to its output maximum of 20 volts peak to peak and the variety of waveforms preloaded on the device. For the two tests, diffuse ultrasound analysis and coda wave interferometry, a square pulse was utilized, which was repeated 50 times at a frequency of 50hz. The individual square pulses had a pulse width of 2.5 microseconds with an amplitude between 2 and 3.5 volts depending on the specimen. Another benefit of this device is its ability to output square waves in groups to assist with averaging over 50 test samples per data set.

3.1.2 Pre-Amplifier – Tabor Electronics 9100A

The pre-amplifier chosen for these experiments was the Tabor Electronics 9100A, which amplifies the input square wave up to 400 volts peak to peak depending on the input amplitude of the wave. The output from this device was sent directly to the excitation transducer. This amplifier was needed as the two chosen transducers have high activation voltages. This device takes the input square wave and increases the peak voltage to, on average, 150 volts which are enough to activate both the 50 and 500 kHz transducers used for coda-wave interferometry and diffuse ultrasound, respectively, all the while keeping the fidelity of the waveform generator’s square pulse.

3.1.3 Transducers

a. Olympus 500kHz

This transducer, used for the diffuse ultrasound, was chosen due to its similarity to the transducer used in the Ahn study. The 500kHz transducer from Olympus produces the high frequency needed for the signal to bounce off the concrete aggregate allowing for the detection of microcracking in the concrete’s microstructure.

b. James NDT 50kHz

The James NDT transducer used for the coda-wave interferometry testing was chosen due to its 50kHz frequency and high power, which gives consistent results for the stress level evaluation of the coda-wave method.

3.1.4 Post-Amplifier – Stanford Research Systems Model 560

The SRS Model 560 amplifier was used as the post-amplifier, allowing for the Picoscope to receive the signal from the receiving transducer. The device has a variable, low noise amplification, which ranges from 1 to 5000 times amplification, along with a high-pass filter, further reducing signal noise. Low signal noise is vital when using such high frequencies in a non-homogeneous material such as concrete. The variable amplification provided by the Model 560 allowed for the received signal to be fine-tuned for greater signal homogeneity between specimen types.

3.1.5 Digital Oscilloscope – PicoScope 4000A

The digital oscilloscope used for these experiments is the PicoScope 4000A, an 8-channel oscilloscope capable of capturing 80 mega-samples per second. The second of these features was the prime reason for this device's selection, as the frequency range for the transducer being used is between 50 and 500 kHz. It was necessary for a very high capture rate. The 80 MS/s capabilities of this oscilloscope allowed for the capture of detailed waveforms from the receiving transducer providing well over the needed Nyquist frequency.

Another benefit of this oscilloscope is its software, which allows for a streamlined capture of data points during the beams' loading and unloading process for scale testing (these beams will be described in detail in chapter four of this document). The features that are essential to these ultrasound experiments are the math channel and trigger features. The math channels of the Picoscope software allowed for waveform averaging before exporting to the processing algorithms, significantly increasing the algorithm's efficiency. The trigger feature allowed for the capture of the returned waveform using the initial pulse from the waveform generator to act as an initial flag, which was routed into the oscilloscope resulting in the capture of the received signal.

3.2. Transducer Bonding and Placement

A primary concern discovered during the early testing stages was the transducers' placement and how they should be bonded to the surface of the concrete specimens. Referencing the Ahn study, the transducer could be placed anywhere between 90mm and 120mm (Ahn, Myoungsu, Popovics, & Weaver, 2019). However, the optimal transducer distance can vary from sample to sample and depends on the amount of energy supplied to the transducer. As for the bonding of the transducers to the concrete surface, there are many methodologies, ranging from traditional ultrasonic couplant to cyanoacrylate glue as used by Ahn. Both variables must be kept constant and chosen to maximize the energy transfer from the transducer through the medium and back to the transducer.

Testing to isolate and identify these variables was performed on a 2-inch-thick slab of unreinforced concrete with no loading applied and a reinforced beam segment undergoing direct compression testing. The method employed to grade the effectiveness of each bonding method and placement distance was to maximize the received waveform amplitude while maintaining signal fidelity and minimizing the factor of post-amplification.

3.2.1 Transducer Bonding

The bonding of the transducers to the surface of the concrete specimens has two metrics for success: how well the method can mechanically couple the transducer to the specimen and how well the method can fill surface voids to prevent unwanted signal variations.

The transducers need to be mechanically coupled with the specimen to allow for proper excitation of the specimen. The variable k represents the coefficient for electromechanical coupling. It can be described mathematically as a function of the mechanical energy transferred into the specimen divided by the electrical energy supplied to the transducer, the exact equation for which can be seen in Equation 4 (Uchino, 2017). By increasing the coefficient of electromechanical coupling, there will be an inherent increase in the energy imparted into the concrete. This will minimize the need for post-amplification of the signal and provide higher fidelity. The bonding method must also be able to support the self-weight of the transducer while still providing electromechanical coupling.

$$k^2 = \left[(1/2)\ (dE)^2/s^E\right] \Big/ \left[(1/2)\varepsilon_0\varepsilon^X E^2\right]$$

Equation 4 Equation for electromechanical coupling

The bonding methods outlined in this section can be separated into assisted and unassisted bonding methods. The assisted bonding mediums are non-hardening and therefore require the use of an external mounting mechanism to hold the transducer to the surface of the specimen. These coupling methods are the ultrasonic gel couplant and petroleum jelly. The unassisted bonding methods are hardening and therefore do not require an external apparatus to affix the transducers to the specimen. These bonding methods are paraffin wax, thickened cyanoacrylate glue, and quick-set epoxy. The results of testing each of these methods will be outlined in the list below.

3.2.1.1 Ultrasonic Gel Couplant

This couplant is the most traditional method of coupling transducers to specimens as it provides excellent void filling. However, it is primarily used in circumstances where the surface of the material being examined is smooth and non-porous. Throughout the testing of this coupling method, one problem remained constant. Concrete, a porous material, constantly leached the water content out of the gel couplant reducing its effectiveness in transferring ultrasound into the concrete specimen. As the testing planned later in the experimental procedure called for long periods of continuous load testing, this factor alone eliminated this couplant type from consideration.

It should be noted that within the time where the gel couplant has not yet deteriorated via lack of water content, the results from ultrasonic testing were very consistent. The couplant also provided excellent signal fidelity and did not require excessive amounts of post-amplification. The signal quality depended on the transducer being affixed firmly to the surface of the specimen with external pressure from the fixture shown in Figure 8.

Figure 7 shows how the amplitude and signal quality drastically decreases after the couplant is left to sit and then retested after 30 minutes. This test was performed with 500kHz transducers placed 2 inches apart with a post-amplification of 100 times.

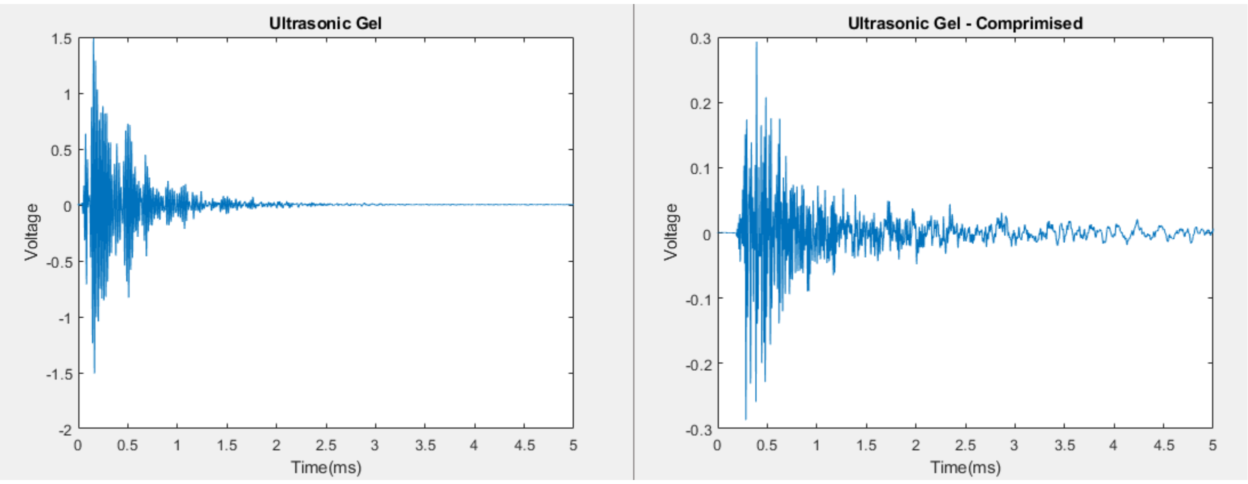

Figure 7 500kHz transducer test 30 minutes apart with ultrasonic gel couplant

The testing with this couplant led to the understanding that a non-water-based couplant would be necessary for ultrasound testing on concrete due to its porous and water leeching tendencies.

3.2.1.2 Petroleum Jelly

Based on the understanding that a non-water-based couplant must be employed for ultrasound testing on concrete, the next step was an oil-based couplant. Petroleum jelly (PJ) was chosen for this application due to its ease of procurement, its inert characteristics, and its similar viscosity to the ultrasonic couplant. Since PJ is a non-hardening bonding solution, an external mount was required to attach the transducers to the surface of the concrete samples. This apparatus was designed using 3-D solid-modeling software and fabricated using a 3-D printer (Figure 8). Figure 8

Figure 8 Example of the external mount for the non-hardening bonding methods with 50kHz transducers

Petroleum jelly has a much longer working time and is suitable for the long-term testing of the small-scale beam. As for the effectiveness in terms of surface void filling and signal quality, the petroleum jelly is on par with freshly applied ultrasonic gel couplant. Figure 9 shows the positive region of two received waveforms using 50kHz transducers with 5x amplification, with the test spaced 24 hours apart. The orange line is the initial test, and the blue line is the second test.

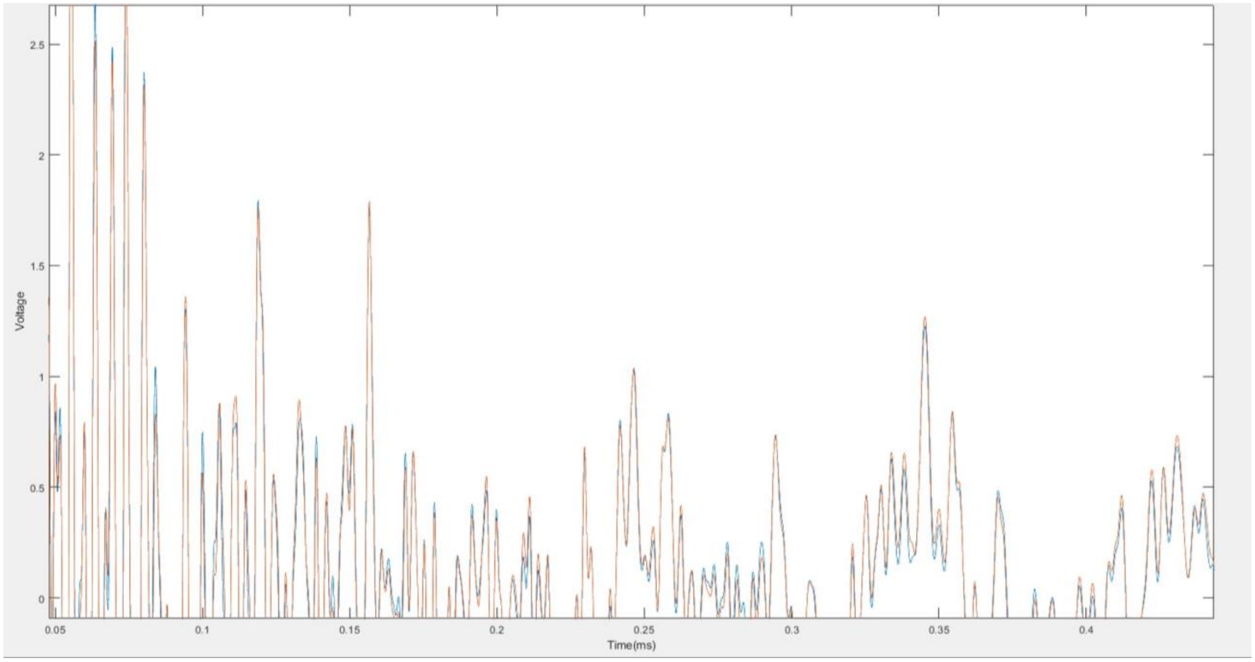

Figure 9 Waveform of 24-hour endurance test for petroleum jelly couplant

The only drawback to testing with petroleum jelly couplant is the lack of self-adhesion to the surface of the specimen. Petroleum jelly requires significant prep work before the transducers can be placed on the surface of the concrete and the feasibility of this method is entirely dependent on the time available and the willingness to affix the mount to the sample permanently.

3.2.1.3 Paraffin Wax

The next step in the bonding experiments is to move onto couplants that can harden and therefore do not need external support to hold the transducers to the specimen. Paraffin wax is a middle ground between non-hardening methods and more aggressive adhesives. Removing the transducers after they are affixed is a simple matter of applying heat to soften the wax. To use the wax on the concrete, it must be first heated to 140 degrees Fahrenheit, which is near the upper limit of temperatures that can cause damage to concrete. Another complication is the rapid solidification of the wax upon contact with the concrete due to the specimen's large thermal mass, which resulted in a short working time. As for the mechanical coupling and signal quality with this bonding method, the paraffin wax was tough to work with and often would result in significant air voids between the transducer and the specimen. This fact, combined with lackluster results from testing, eliminated this bonding method from further testing.

3.2.1.4 Thickened Cyanoacrylate Glue

A thickened cyanoacrylate glue is chosen as the next medium to evaluate in the unassisted bonding method category. Advantages of this medium include a 15-minute working time and its ability to be de-bonded using acetone.

The concrete surface needed to be smoothed using sanding disks for proper adhesion when using the thickened super glue. Without proper sanding, the pits in the concrete surface would not be filled by the couplant, and the waveform would not be effectively transmitted into the specimen. Also, as a compressive load is applied to a specimen where the super glue is being utilized, the couplant tends to fail, allowing for the transducer to decouple from the specimen.

Even when the thickened cyanoacrylate glue is used under perfect conditions, the received signal is still weak and lacks distinct signal features. The glue layer between the transducer and concrete is too thick and has a varied density, which impedes ultrasound transmission through the specimen. An example received waveform from an ideal test with a 50kHz transducer setup with an unamplified input amplitude of 3 volts, compared to a standard 2 volts, can be seen in Figure 10.

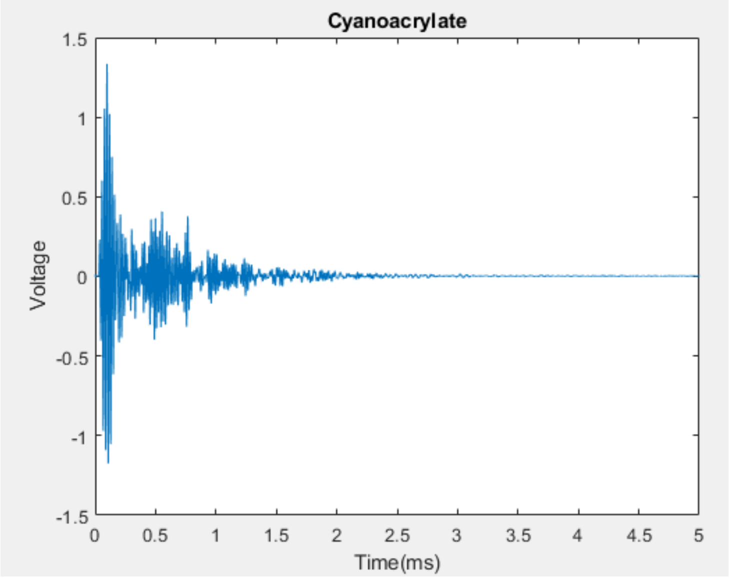

Figure 10 Waveform from Cyanoacrylate couplant testing

As seen in Figure 10, the maximum amplitude of the waveform is like the expected 1.5 volts as seen from the traditional ultrasonic gel couplant. The returned waveform’s proper amplitude was achieved with a higher-than-normal input amplitude of 3 volts. The signal fidelity was high, and the waveform shape was also proper.

Overall, the main reasoning behind this method not being further explored throughout the small-scale testing was the lack of reliability when applying loads to the specimens. Without confidence that the transducers can be coupled throughout loading cycles, this couplant was deemed unsuitable for the applications in this study.

3.2.1.5 Quick Set Epoxy

An ordinary quick set epoxy was chosen to remedy the issues faced while testing the thickened cyanoacrylate glue. Epoxy was not the first choice when looking at the mechanical coupling of the transducers to concrete because of the permanent nature of epoxy. A sizeable force must be applied to break the bond to remove the transducers from the specimens' surface. In the case of the testing performed during the bonding tests, a piece of wood and a mallet were used to shear the transducers off the face of the sample when the testing came to completion.

The quick-set epoxy held the transducers firmly to the face of the concrete with no issues of decoupling. The signal fidelity during testing with the epoxy was high, with little amplification needed for either the 50 or 500kHz transducers. This coupling method provided consistent results while load testing and has no deterioration over time like other coupling methods. This method was selected for testing the scale beam specimens produced for this study due to its simple effectiveness and ability to have consistency across multiple loading tests.

3.2.2 Transducer Placement

Placement of the transducers has important effects on the resulting waveform received for processing. The further away the transducers are from each other, the less energy is directly received, but in trade, there is more scattering, resulting in more apparent feature characterization. The initial placement of the transducers came from the Ahn study, describing 90mm to 120mm between transducers (Ahn, Myoungsu, Popovics, & Weaver, 2019). However, some studies, such as the one by Deroo, recommend a planar distance of as little as 46mm between transducers (Deroo, Kim, Qu, Sabra, & Jacobs, 2010). The Zhang study proposed placing the transducers across from each other on the sample (Zhang, et al., 2012). The Larose study further endorsed the cross method where transducers were placed across from one another for CWI testing (Larose & Hall, 2009)

As for the diffuse ultrasound setup using the 500kHz transducers, a cross method is being implemented due to the experimental success found in these preliminary experiments, along with the prior endorsement by both the Zhang and Larose studies.

For the coda-wave interferometry testing, a planar approach will be taken. Though the two studies by Ahn and Deroo use small distances between their transducers, the experiments on the small-scale specimens in this study will be spaced at 4 inches from the center. The larger spacing is because the transducers used in these experiments are higher energy and can be placed further from one another without a penalty to the received signals. The increased spacing promotes flexibility while testing small-scale beams, mainly allowing the placement of transducers on either side of the loading head in the 3-point loading test.

3.3. Data Processing

Two separate algorithms exist for processing the diffuse ultrasounds and coda-wave interferometry. Both algorithms were implemented in MATLAB and function independently. The process and background for creating these algorithms are described in sections 3.3.1 and 3.3.2.

Each time the transducers are fired, 50 samples will be collected and averaged, resulting in a single waveform with decreased noise. The waveforms will be averaged before being passed into the algorithms for additional processing.

3.3.1. Diffuse Ultrasound

The goal of the data processing for the diffuse ultrasound method is to isolate the diffusivity and dissipation coefficients for each dataset. The coefficients from tests at differing points can provide insight into the state of microcracking in the samples. An increase in microcracking can indicate that the PT system is undergoing damage.

3.3.1.1. First Iteration

The inspiration for the first method employed to find the coefficients of diffusion and dispersion came from the Ahn study. This processing technique is in the flowchart shown in Figure 3, which consists of a time-frequency analysis of the data.

The first step following averaging the data set is to perform a fast Fourier transform on the data. The Fourier transform changes the data from a time domain to a frequency domain. From here, the program will apply a Hanning window to the transformed data set to isolate three frequency windows, 200-300kHz, 300-400kHz, and 400-500kHz. The program then uses an inverse Fourier transform on the windowed signals in the frequency domain to bring them back to a time domain. Then windowed signals back in the time domain are converted to their absolute value and squared; the absolute value and squaring results in a plot of the ultrasounds energy density with respect to time. The algorithm then takes the logarithmic form of the energy density dataset per windowed section. The logarithmic form of the energy density of each frequency window is then curve fit to the diffuse ultrasound equation in Equation 5. The curve fitting provides solutions for the coefficients of dissipation and diffusivity, allowing for the characterization of microcracking in the test sample.

$$\log\langle E(x,y,z,t)\rangle = C_0 - \frac{3}{2}\log(Dt) - \frac{d^2}{4Dt} - \sigma t$$

Equation 5 Diffuse ultrasound equation used by Ahn for curve fitting windowed energy density plots (Ahn, Myoungsu, Popovics, & Weaver, 2019)

The first iteration of the diffuse ultrasound processing algorithm provided inconsistent data when comparing the energy density of the frequency windows. Instead of the energy density of the windowed frequency ranges following a decreasing energy density trend as the frequency increased, the energy density stayed similar across all frequency windows. Figure 11 shows the overlap of the energy density per windowed section.

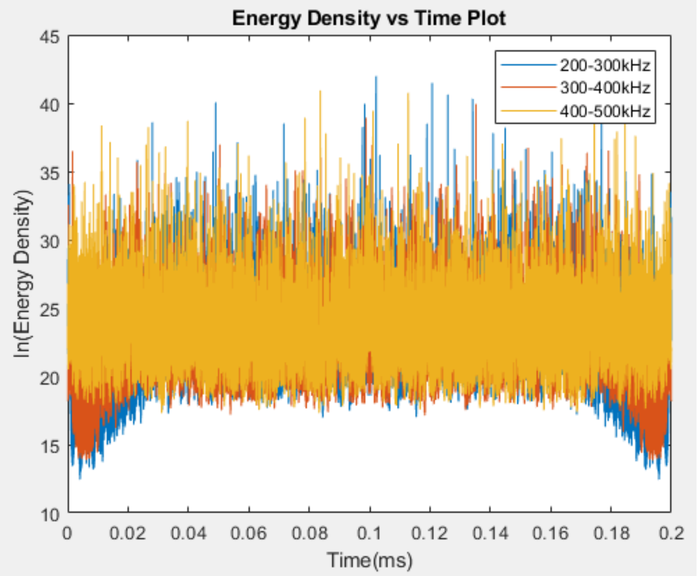

Figure 11 Diffuse Ultrasound Algorithm First Iteration Energy Density vs. Time Plot

The most likely culprit of the non-distinct frequency bands is that the Fourier transform was being applied to the whole signal simultaneously. The second iteration of this program with a varied approach to using the Fourier transform was necessary.

3.3.1.2. Second Iteration

The second iteration of the diffuse ultrasound algorithm begins with the aim of finding a solution to the equation in Equation 2. To calculate the coefficients of diffusivity and dissipation and to curve fit the equation, the algorithm divides the averaged signal received from testing into time intervals of 50 microseconds with 90% overlapping the previous interval. The program takes the integral of the particular time intervals over the frequency bandwidth of interest, in this case, 500kHz. The energy density of each time interval is associated with the instant of time at the center of the interval. The algorithm then plots the values of energy density with respect to time. Curve fitting of the diffuse ultrasound equation to this plot will find the coefficient for both dissipation and diffusivity. The two coefficients will identify trends in microcracking of the specimens during testing.

This algorithm has proven to work effectively in finding both coefficients of interest. Therefore, the small-scale testing with direct compression and 3-point beam load testing will use this version.

3.3.2. Coda-Wave Interferometry

The algorithm for identifying the time lag of concurrent datasets to perform CWI is a more straightforward process than that of diffuse ultrasound. The first iteration of this algorithm worked as planned and therefore did not need a revision.

The algorithm first ingests a series of files correlating to one cyclical loading test of the small-scale specimens. The algorithm places the ingested files in order, then a time interval corresponding to the waveform area representing the clearest delay between wave arrivals is taken and linked to its corresponding load. The program uses a cross-correlation function based on the one seen in Equation 3, correlating each progressive load increase and eventual decrease to the initial zero load reading. The algorithm then calculates the percent change of the wave velocity for quantification of concrete damage. The plot of the relative velocity change vs. the corresponding load values shows the trend of increasing time lag when the sample is in tension and decreasing time lag when the sample is in compression (Gondim & Haach, 2021).

Initial testing with this algorithm shows linear relationships between an increase in tension and an increase in time for the coda-wave to arrive. Features also appear when expected, such as jumps in the time lag when cracking or yielding occurs. The CWI algorithm described in this section is used in further testing on small-scale specimens in this study due to the success in preliminary testing.

3.4. Test Specimens

The experiments for this study will begin with the creation of three specimens for testing and verification of the diffuse ultrasound and coda-wave interferometry methods. These testing methods will be direct compression testing, 3-point load testing of a simply reinforced beam, and 3-point load testing of a post-tensioned beam with plain reinforcing.

The direct compression testing will involve a 12-inch cut section from a 5-foot beam identical to the one used in the 3-point load testing. A Tinus and Olsen universal testing machine will be applying loading to the beam cutting, which is on its end. The petroleum jelly bonding method with external mounting holds the 50kHz transducers in a planar configuration with 4 inches of separation and the 500kHz transducers at a cross configuration across the beam center.

The normally reinforced 3-point load testing will occur on a 5-foot long beam with a 4.75x3.5-inch cross-section. The beam reinforcement consists of four #3 bars and shear reinforcement via 14 eight-inch stirrups at 1.75-inch spacing on each beam side. Epoxy bonds the 50 and 500kHz transducers, with the 50kHz transducers centered on the beam with 4-inch spacing and the 500 kHz transducers placed in the cross configuration at the beam's center point. A Tinus and Olsen universal testing machine and a 3-point load testing frame will be the apparatus used for the beam loading (Figure 12).

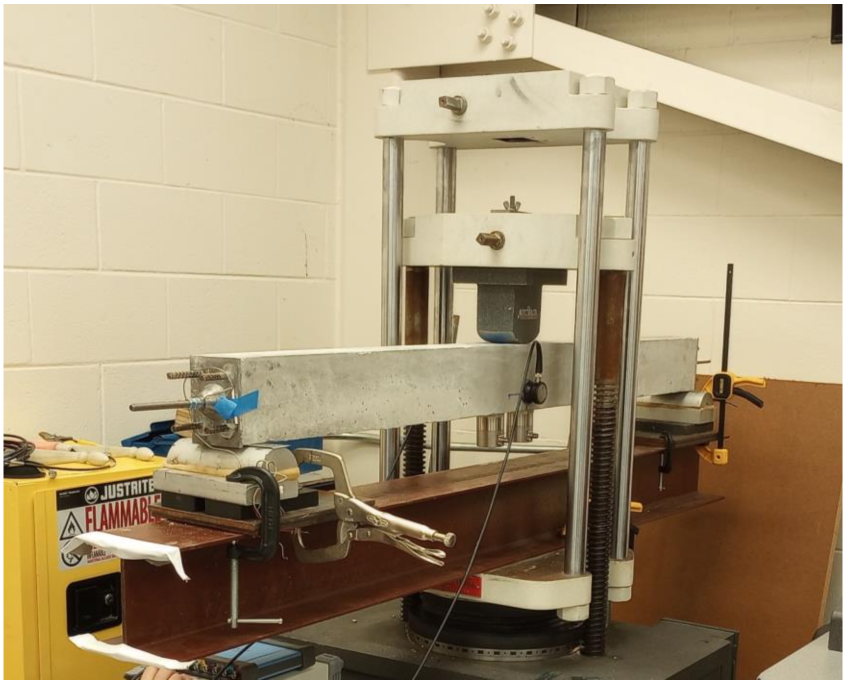

Figure 12 Image showing the 3-point load testing frame and the Tinus and Olsen universal testing machine

The post-tensioned 3-point load testing will also occur on a 5-foot long beam with a 4.75x3.5-inch cross-section. The beam reinforcement consists of four #3 bars and shear reinforcement via 14 eight-inch stirrups at 1.75-inch spacing on each beam side with the addition of a 3/8 inch threaded rod for post-tensioning. The application of post-tensioning force via the tightening of two nuts on either end of the beam is quantified by a load cell sandwiched between the metal plate on the beam end and the nut used for tensioning. The epoxy bonding method will be utilized for the 50 and 500kHz transducers, with the 50kHz transducers centered on the beam with 4-inch spacing and the 500 kHz transducers placed in the cross configuration at the beam's center point. A Tinus and Olsen universal testing machine and a 3-point load testing frame will be the apparatus used for the beam loading (Figure 12).

Chapter 4: Experimental Work

In the initial planning stages for this study, both small-scale and full-scale experiments were intended to be completed. However, time constraints applied due to the COVID-19 pandemic meant that the full-scale experiments could not be conducted. Therefore, the extent of the experimental works for this was limited to small-scale testing of the two methods. The general plans for full-scale testing will be discussed as a direction for possible future work.

4.1. Small Scale Specimens

The small-scale testing for all specimens was performed using a Tinius Olsen universal testing machine to apply load. The data was captured from the transducers using the Picoscope software packaged with the digital oscilloscope. Each small-scale specimen was broken into testing groups by specimen type/test type; these testing groups were further broken down into loading cycles. The naming convention for each test will follow the format of (Testing Group).(Loading Cycle).

4.1.1. Beam-blocks

Testing for the beam blocks involved data collection for the diffuse ultrasound and coda-wave interferometry methods. Both transducer sets were attached to the beam blocks using an external mounting bracket with petroleum jelly as the coupling medium. The 50kHz transducers were affixed to the 4.75-inch-wide face of the blocks in a planar configuration at a distance of 4-inches. The 500kHz transducers were placed across the thin distance of the block at the bottom of the beam.

The load testing procedure involved two loading cycles of interest, one with the 50 kHz transducers and one test with the 500kHz transducers. These direct compression tests, performed in the Tinus and Olsen machine, applied force to the specimen in 1,500-pound increments; at each increment, a transducer pulse was fired, and a set of data was collected until a peak loading of 15,000 pounds was reached. At this point, the sample was unloaded at increments of 3,000 pounds; again, a transducer pulse was fired, and data was collected at each increment until 0 pounds of force was applied to the sample. This exact procedure was followed for each of the two tests, one 50kHz test followed by a 500kHz transducer test. These tests are labeled as 1.1 and 1.2; the first number relates to the testing group, and the second is the test's time-correlated place in the group. The specific settings used with the equipment can be seen in Table 1, and an image of the testing setup can be seen in Figure 13.

Parameters	**50 kHz Test (1.1)**	**500 kHz Test (1.2)**
Unamplified Pulse Amplitude (V)	3	2.5
Pulse Width (μs)	2.5	1
Post-Amplification	1	100
Number of Pulses	50	50
Frequency of Pulses (Hz)	50	50
Sampling Rate (MS/s)	10	10

Table 1 Parameters for 50 and 500 kHz testing on Block Specimens

Figure 13 Testing setup for small-scale block testing

4.1.2. Beams

The scale-beam testing applied the same principles as block testing. The specimen is loaded and unloaded in increments with transducer pulses, and data is collected at each point. For the scale beams, the transducers, both 50 and 500 kHz, were epoxied directly to the face of the beam. The loading increments for each beam and loading cycle varied from test to test, though the parameters for the recording equipment stayed mostly steady across all trials. The testing was completed using the Tinus and Olsen machine and a 3-point load testing frame. The frame consisted of a steel beam with metal rollers on each end corresponding to the end of the small-scale concrete beams and a rounded loading head at the center point of the beam.

4.1.2.1. Simply Reinforced

Testing on the small-scale simply reinforced beam involved diffuse ultrasound and coda-wave interferometry methods with one diffuse ultrasound test and three coda-wave interferometry tests for a total of 4 tests. The 50kHz transducers were centered on the bottom of the beam with 4-inches of center-to-center spacing. The 500kHz transducers were placed at the bottom center of the beams' sidewall. As stated previously, all transducers were epoxied directly to the surface of the beam. The setting used on the data collection equipment for the load testing can be found in Table 2.

Parameters	**50 kHz Test (2.1)**	**500 kHz Test (2.2)**	**50kHz Tests (2.3, 2.4)**
Unamplified Pulse Amplitude (V)	3	2.5	3
Pulse Width (μs)	2.5	1	2.5
Post-Amplification	5	100	1
Number of Pulses	50	50	50
Frequency of Pulses (Hz)	50	50	50
Sampling Rate (MS/s)	10	10	10

Table 2 Data collection parameters for simply-reinforced beam load testing

Load test 2.1 involved 50kHz transducers and a loading increment of 50 pounds until 350 pounds and unloading at 50-pound increments until 0 pounds; this loading cycle was performed twice. Load test 2.2, involving the 500kHz transducers, followed the same loading cycle as test one. Load test 2.3 aimed to bring the beam to a state of cracking and followed a loading increment of 100 pounds until 400 pounds, then an increment of 50 pounds until 3,000 pounds; the unloading process involved 200-pound increments until the beam was completely unloaded. Load test 2.4 aimed to load the beam until yielding; therefore, the increment of loading was 100 pounds until 3,100 pounds, then 50 pounds until 3,350 pounds; the unloading of the beam followed in increments of 100 pounds until fully unloaded. For tests 3 and 4, displacement data for the loading cycles was also taken to correlate later to the coda-wave interferometry data.

4.1.2.1. Post Tensioned

Testing for the small-scale post-tensioned beam occurred in two portions, tensioning of the beam and 3-point load testing. For both test modes, the transducers, both 50 and 500kHz, were coupled to the surface of the beam using epoxy. The placement of the transducer was identical to the plain reinforced beam and is as follows. The 50kHz transducers were centered on the bottom of the beam at 4-inches from the center. The 500kHz transducers were placed at the bottom center of the beams' sidewall. The 3-point testing was completed using the Tinus and Olsen machine and a 3-point load testing frame. The frame consisted of a steel beam with metal rollers on each end corresponding to the end of the small-scale concrete beams and a rounded loading head at the center point of the beam.

The post-tensioning for this small-scale beam was accomplished by tightening a threaded rod placed through the center of the beam. The tensioning cycle was measured using a force cell placed on the threaded rod (Figure 14), which was connected to a multimeter for tension readings.

Figure 14 Picture showing load cell used for post-tensioning measurements on scale-beam

The loading cycle 3.1 tensioned the rod in increments of 1000 pounds from 0 to 7000 pounds and then de-tensioned to 1000 pounds, then increased tensioning to 8000 pounds in 1000 pound increments. For each increment of the tensioning cycle, the 50kHz transducers were used to collect data for coda-wave interferometry testing. The data collection equipment settings can be seen in Table 3.

Parameters	50 kHz Tensioning Tests (3.1)
Unamplified Pulse Amplitude (V)	2
Pulse Width (µs)	2.5
Post-Amplification	5
Number of Pulses	50
Frequency of Pulses (Hz)	50
Sampling Rate (MS/s)	10

Table 3 Parameters for data collection for small-scale tensioning tests

For the 3-point load testing of the PT-beam, a total of 5 trials were performed, 4 with the 50kHz transducers and 1 with the 500 kHz transducers. The first test, 4.1, was conducted with the 50kHz transducers; the loading was applied and then unapplied at increments of 50 pounds from 0 to a maximum of 350 back down to 0 pounds. The second test, 4.2, was conducted with the 500kHz transducers; the loading was applied and then unapplied at increments of 50 pounds from 0 to a maximum of 350 back down to 0 pounds. The third test, 4.3, utilized the 50kHz transducers; the loading increment for the test was 50 pounds from 0 to 350 back to 0 pounds. Test 4.4 used loading increments of 100 pounds up to a maximum of 1200 pounds, then increments of 200 pounds down to 0 pounds of force. At this point, one of the coils inside the main pre-amplifier burnt out, and a similar replacement was sourced to conduct the final two tests. The replacement pre-amplifier was calibrated to mimic the original device’s amplification perfectly. The fifth test, 4.5, aimed to bring the beam to a state of cracking; therefore, the loading reached a maximum of 2,200 pounds at an increment of 100 pounds; the beam was then unloaded at an increment of 200 pounds until it was completely unloaded. For all tests on the PT-beam displacement, measurements were taken simultaneously with the test. Figure 15 provides an image of the beam setup, and Table 4 will give the parameters used in the data collection equipment for all tests.

Figure 15 Picture showing the 3-point load testing setup for the PT-scale-beam

Parameters	**50 kHz Tests (4.1, 4.3, 4.4, 4.5)**	**500kHz Test (4.2)**
Unamplified Pulse Amplitude (V)	2.5	2.5
Pulse Width (µs)	2.5	2.5
Post-Amplification	5	20
Number of Pulses	50	50
Frequency of Pulses (Hz)	50	50
Sampling Rate (MS/s)	10	10

Table 4 Data collection parameters for load testing the small-scale PT-Beam

4.2. Large Scale Specimens

Due to time constraints, large-scale testing could not be included in this study. However, the general framework for implementing diffuse ultrasound and coda-wave interferometry in large-scale specimens will be discussed for the benefit of future studies.

For any large-scale beam-type specimen, it would be recommended that both 50 and 500kHz transducers be epoxied to the centermost point of the tension critical face. The spacing between 50kHz transducer would be consistent with the small-scale testing at 4-inches of center-to-center space. For 500kHz transducers, instead of being placed in a cross configuration like in small-scale testing, they would be placed on the tension face of the beam like the 50kHz transducers; the spacing for the 500kHz transducers would need to be smaller than their counterparts due to their lower energy nature. Therefore, a spacing of 2-inches center to center would be recommended for the 500kHz transducers.

The data collection equipment would be identical to the small-scale experiments discussed in this report. The setting used, such as amplitude, amplification, and pulse width, may need to be adjusted according to the size and material properties of the specimen. The method of load testing would need to be scaled in accordance with the size of the full-scale specimen along with the load increments used. Aside from these differences, the testing methods follow the same trends as those described in the small-scale testing section of this chapter.

Chapter 5: Results and Discussion

5.1. Coda-Wave Interferometry

The outcomes being sought for Coda-wave interferometry for the NDE of PT flexible filler systems is an indirect evaluation of the health of the post-tensioning system. For CWI, this means having damage feature recognition from the stress level and, therefore, the phase shift of waves being passed through the specimen. These features can either be the identification of substantial cracking or yielding of the materials in the flexible filler system. The specimens used for these tests and testing procedures are outlined in detail in Chapter 4 of this document.

5.1.1. Beam Block Testing

The beam block specimens' testing will show the general feasibility and efficacy of the CWI testing setup for identifying damage features relevant to flexible filler PT systems. These features would be identified via the relative velocity change plots generated by the CWI algorithm and would take the form of deviations in the slope or shape of the plots.

1. Test 1.1

The importance of Test 1.1, whose results can be seen in Figure 16, is the movement of the relative velocity change in the negative direction during direct compression loading, the consistent slope change with progressive loading, and the clear differentiation between the starting and ending points of the loading cycle. The velocity variation is expected to move in the negative direction when in compression as the wave properties predict faster arrival times when a specimen is experiencing compression. This effect is clearly shown in the plot for Test 1.1 and, therefore, is the first step in validating the effectiveness of the testing setup. The plot’s curved shape and the shifted endpoint compared to the initial test point show the expected effect of the concrete’s memory of damage. The general trend of the increasing slope with respect to increasing stress further proves that the testing setup used for CWI in this study is operating correctly and therefore is applicable to further use on small-scale specimens.

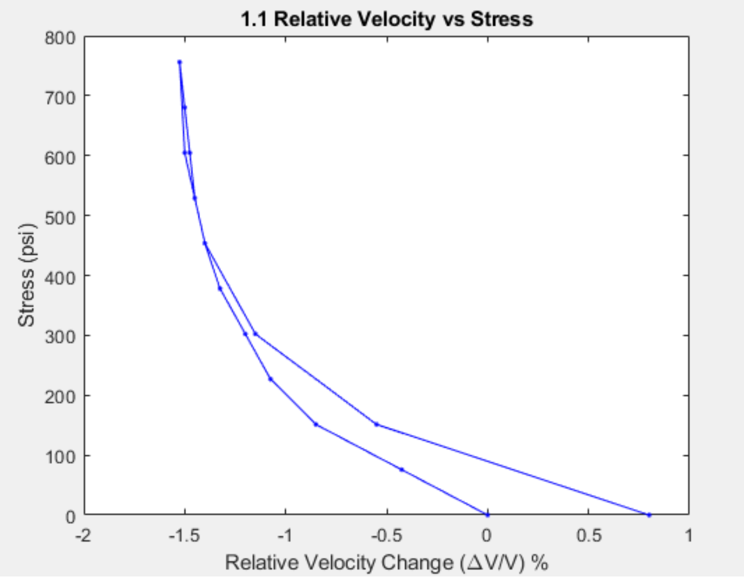

Figure 16 Small-scale Beam-block, Direct Compression, Coda-wave Interferometry Test 1.1 - Graph of Relative Velocity vs. Stress

5.1.2. Beam Testing

After validating the testing setup with the beam block testing, the next step is small-scale beam testing in both normally reinforced and PT beams. These beams will undergo 3-point load testing, described in Chapter 4. In these tests, the same damage features as the beam blocks are expected to appear in addition to possible cracking and yielding of the beams. These damage features are expected to cause dramatic changes in the relative velocity change vs. load plots and, in a real-world application, point to the deterioration of the PT flexible filler system.

5.1.2.1. Normally Reinforced

1. Test 2.1

This test acted as the preliminary validation for the application of the transducers to the new specimen and the 3-point load test on the beams. This test consisted of a two-cycle loading, reaching approximately 350 psi each time. This loading was chosen due to its probability of not cracking the specimen in any way, allowing for direct comparison between the cycles. The plot shown in Figure 17 shows the relative velocity change vs. stress plots for both load cycles. As expected, the two plots mimic each other near-perfectly aside from the shifting caused due to concretes tendency to have a memory for loading and damage. The damage most likely to be causing the shift would be microcracking caused by the first load cycle.

It should be noted that as the stress increases, the relative velocity change moves in the positive direction. This shift indicates the area in which the transducers are placed in tension. This indication is correct as the transducers are placed on the bottom of the beam, which undergoes tension when in a 3-point load test. The repeat nature of the shifts in the expected direction proves both the CWI setup’s efficacy on the beam specimens and foreshadows that if extensive damage such as cracking or yielding should occur, then there will be a significant observable change in the plots.

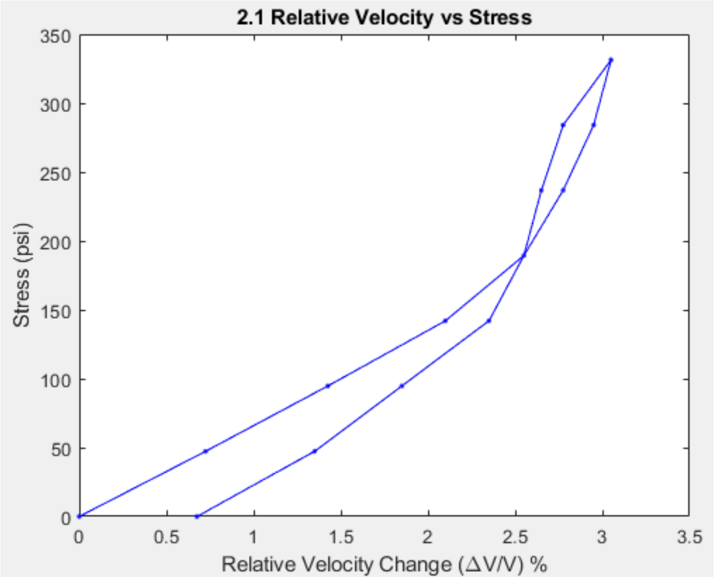

Figure 17 Small-scale Normally Reinforced Beam, 3-Point Load, Coda-wave Interferometry Test 2.1 - Graph of Relative Velocity vs. Stress

2. Test 2.3

The purpose of Test 2.3 was to bring the normally reinforced beam to the point of cracking, which would hopefully reflect on the relative velocity change plot. For this test, displacement data for the loading cycle was also collected to be compared to the relative velocity change plot to coordinate signal features. As shown in Figure 18, as the stress applied to the beam approaches 2500 psi, the displacement vs. stress graph data shows a slight shift reflected in the relative velocity change plot by a sizeable horizontal change between data collection points. This shift points to the onset of cracking in the specimen, which is confirmed by the effect on the displacement plot. As expected, when this cracking occurred, the time taken for the waveform to travel between transducers was slightly increased, resulting in a significant shift in the relative velocity.

Another relevant feature of this plot is the significant shift between start and end points, which confirms that CWI is sensitive to the effects of compression and tension over time and damage to the specimen.

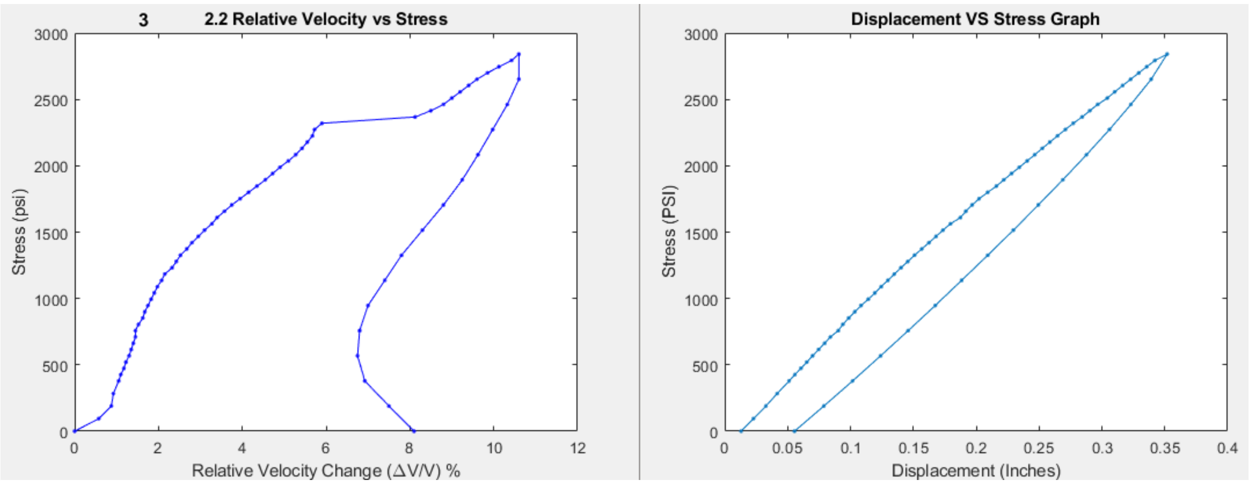

Figure 18 Small-scale Normally Reinforced Beam, 3-Point Load, Coda-wave Interferometry Test 2.3 - Graph of Relative velocity change vs. Stress and Displacement vs. Stress

3. Test 2.4

After Test 2.3, the next logical step would be to observe beam yielding, which is the goal of Test 2.4. This test will hopefully show a drastic and varied response to the yielding of the beam when compared to cracking, which was observed previously. The results of Test 2.4 can be seen in Figure 19 and show the expected harsh response to yield. As the stress approaches and exceeds, 3000 psi, an evident change in the displacement plot is seen, which is a clear sign of yielding due to the drastic slope change. The change in the displacement plot is reflected even more drastically in the relative velocity change vs. stress plot; as 3000 psi of stress is reached, the relative velocity change becomes near horizontal over the remainder of the increasing load portion of the test. This signal feature should be easily identified in further tests and is varied enough from the feature caused by cracking.

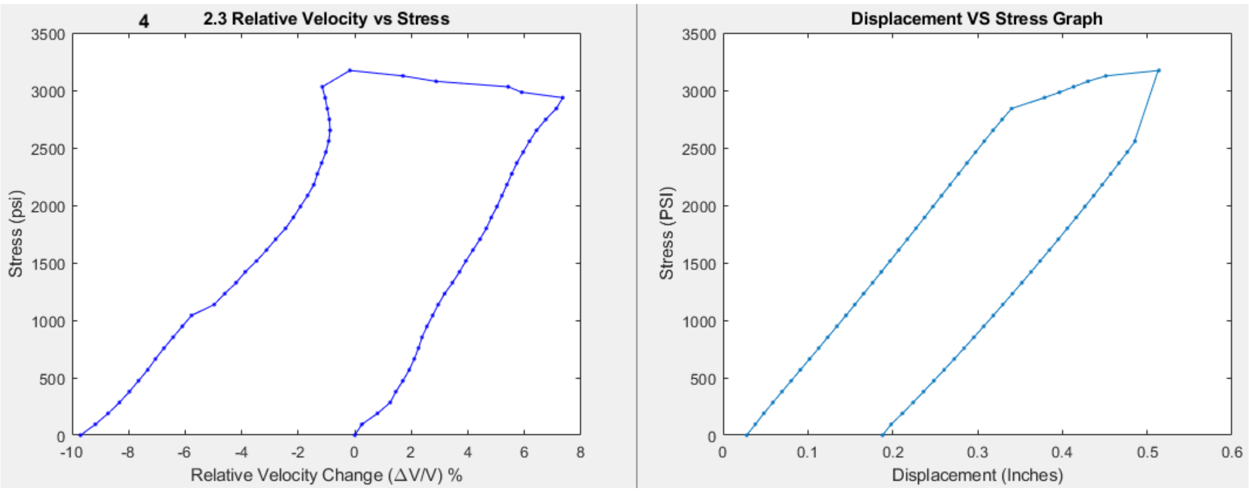

Figure 19 Small-scale Normally Reinforced Beam, 3-Point Load, Coda-wave Interferometry Test 2.4 - Graph of Relative velocity change vs. Stress and Displacement vs. Stress

5.1.2.2. Post Tensioned

1. Test 3.1

The first test for the PT scale beam involved the tensioning process outlined in Chapter 4. This test was implemented to validate the sensitivity of CWI to the tensioning and de-tensioning of a simulated PT strand, which is a full-scale application that could be an indicator of PT failure. This observation was successful, as can be seen in Figure 20. The relative velocity change plot vs. the loading moved in the negative direction during tensioning and in the positive direction during de-tensioning, which was as expected. Also, the second tensioning brought the beam up to the final 400 psi of PT force, closely following the slope and shape of the first cycle up until the previous maximum. This provides a positive insight into the consistency and sensitivity of the CWI method to the application and removal of post-tensioning force.

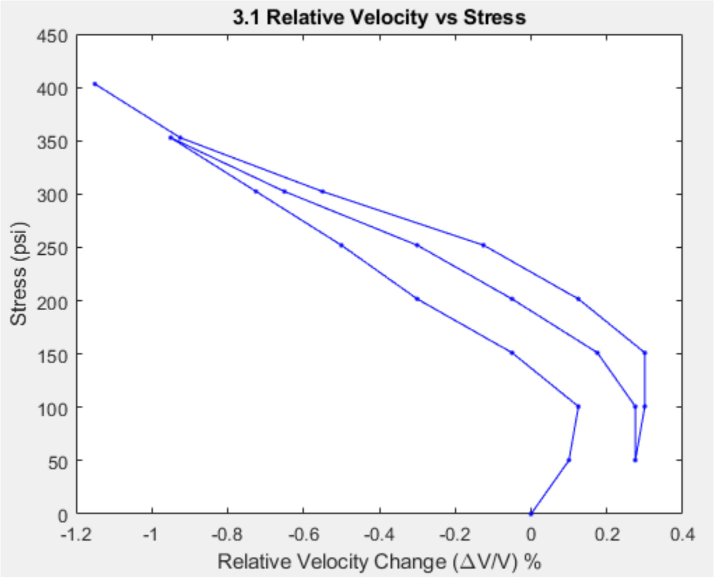

Figure 20 Small-scale PT Beam, Tensioning, Coda-wave Interferometry Test 3.1 - Graph of Relative velocity change vs. Stress

2. Test 4.1

The first of the 2-point load tests on the PT small-scale specimen were test 4.1, which had the goal of matching the displacement vs. stress plot to the relative velocity change vs. stress graph for use as a control to compare against damage features caused by excessive loading. Both plots in Figure 21 follow the same trends as the normally reinforced beam, which underwent the loading process with one key distinction. The distinction is the reduction in the shift between starting and ending points. This is expected as the post-tensioning present in this specimen serves to increase the elastic nature of the specimen. Furthermore, this test proves the proper attachment of the transducers to the beam and application of CWI to this specimen by the closely matched plots of the displacement vs. stress and relative velocity change vs. stress plots.

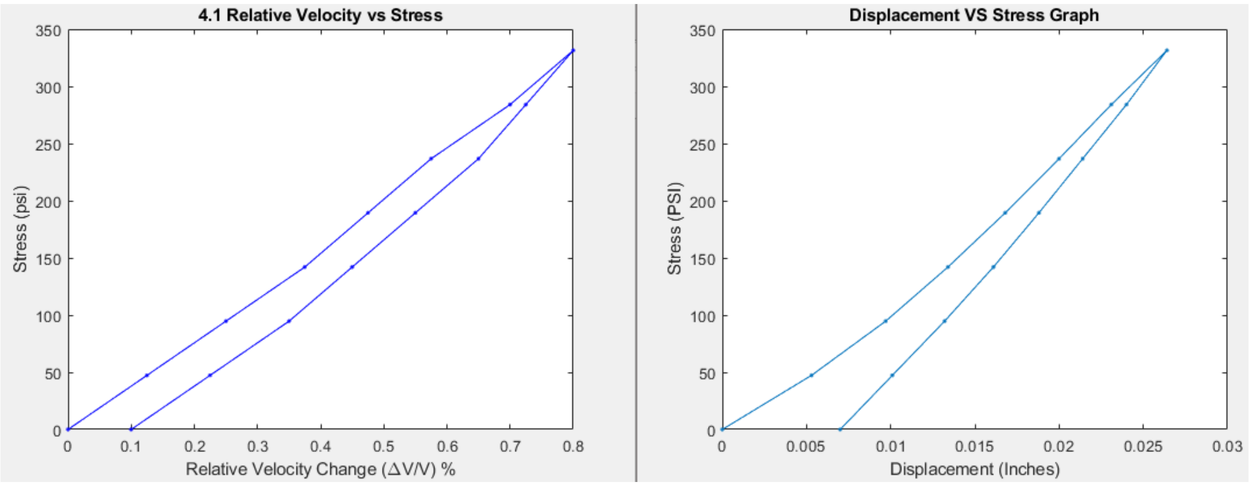

Figure 21 Small-scale PT Beam, 3-Point Load, Coda-wave Interferometry Test 4.1 - Graph of Relative velocity change vs. Stress and Displacement vs. Stress

3. Test 4.3

This test is a direct recreation of test 4.1 with no test before it reaching above a maximum of 350 psi. The results shown in Figure 22 illustrate the same outcomes as Test 4.1 and validate the effectiveness and repeatability of CWI. As seen previously, the displacement vs. load and relative velocity change vs. stress plots follow the same slope and shape trends as expected from the previous testing. No evidence of additional damage to the concrete could be witnessed, which is expected due to no extreme loading being applied before this test.

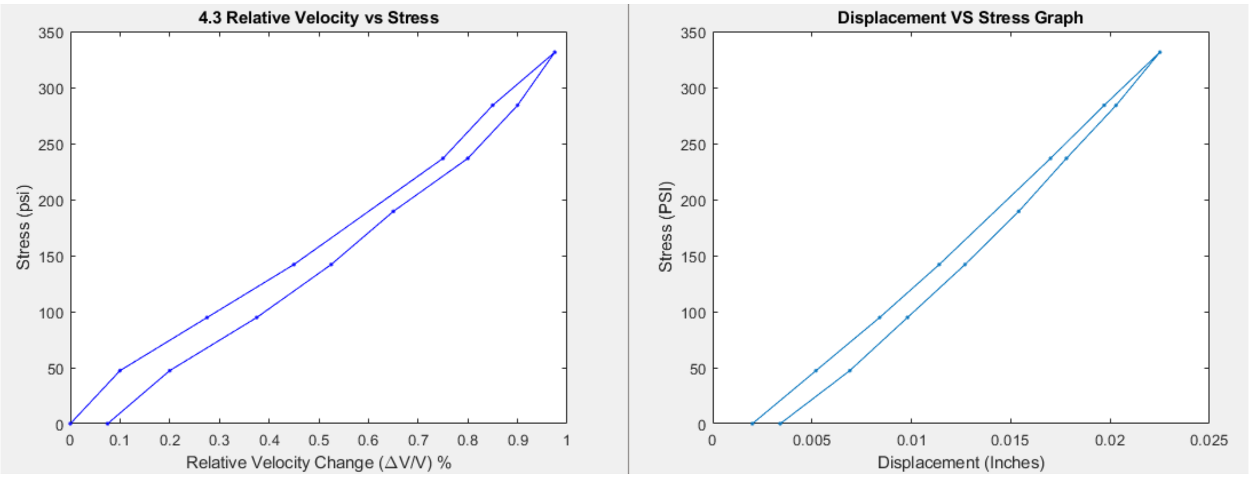

Figure 22 Small-scale PT Beam, 3-Point Load, Coda-wave Interferometry Test 4.3 - Graph of Relative velocity change vs. Stress and Displacement vs. Stress

4. Test 4.4

Following the normally reinforced scale specimen testing, this test will seek to increase loading to identify damage features in the plots. Figure 23 shows the displacement plots and relative velocity change vs. stress. Contrary to the normally reinforced beam, the two plots do not follow each other for the entirety of the loading cycle; instead, as the loading approaches and exceeds 600 psi, the relative velocity change plot begins a vertical trend. This trend can be attributed to the post-tensioned reinforcement being mobilized, resulting in less and less tension in the bottom-most portion of the beam where the transducers are placed. Since the maximum stress of 1200 psi did not yet reach the calculated cracking point of this specimen, there is no damage feature found on the plots of either displacement or relative velocity change.

This test proves a distinction between the mobilization of PT reinforcement and actual damage features, which would display on the output relative velocity change plot as a nearly horizontal line. Another notable outcome is the small shift in the relative velocity change between starting and ending points which is consistent with what is expected of PT reinforced beams and specimens. As stated in the results of Test 4.1, the PT reinforcement provides more elasticity to the beam allowing for a closer return to the original state of the beam prior to loading when compared to a non-post-tensioned specimen.

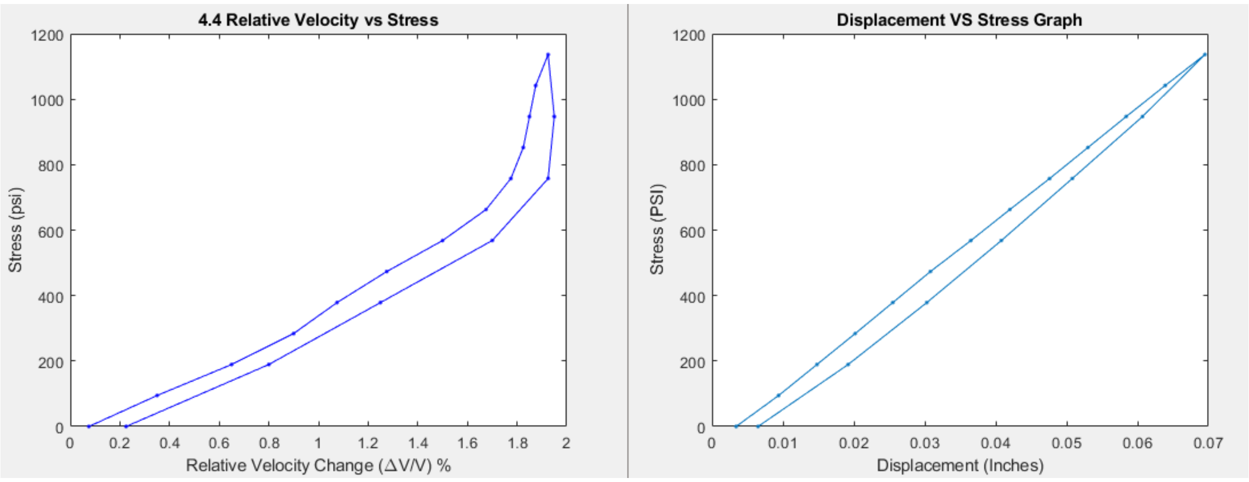

Figure 23 Small-scale PT Beam, 3-Point Load, Coda-wave Interferometry Test 4.4 - Graph of Relative velocity change vs. Stress and Displacement vs. Stress

5. Test 4.5

The final test on the small-scale PT specimen aimed to induce cracking within the specimen; yielding was not explored for this specimen due to the large load expected to be required to do so. Figure 24 shows the displacement and relative velocity change vs. stress plots. These plots both show damage indicators for cracking; the displacement plot shows a starting at 1500 psi, indicating that cracking occurs in the beam. As experienced with the normally reinforced beam, the coinciding effect on the relative velocity change plot is significantly more prominent. As experienced in Test 4.4, there is a near-vertical slope of the line while the PT reinforcement is being mobilized, and then as the beam is cracked, there is a horizontal trend to the plot. This change in the slope proves the variation between the two effects and can be used effectively to identify the two features. Though not tested, it would be expected for the yielding of the beam to provide a longer lasting and more prominent horizontal trend in the relative velocity change vs. load plot.

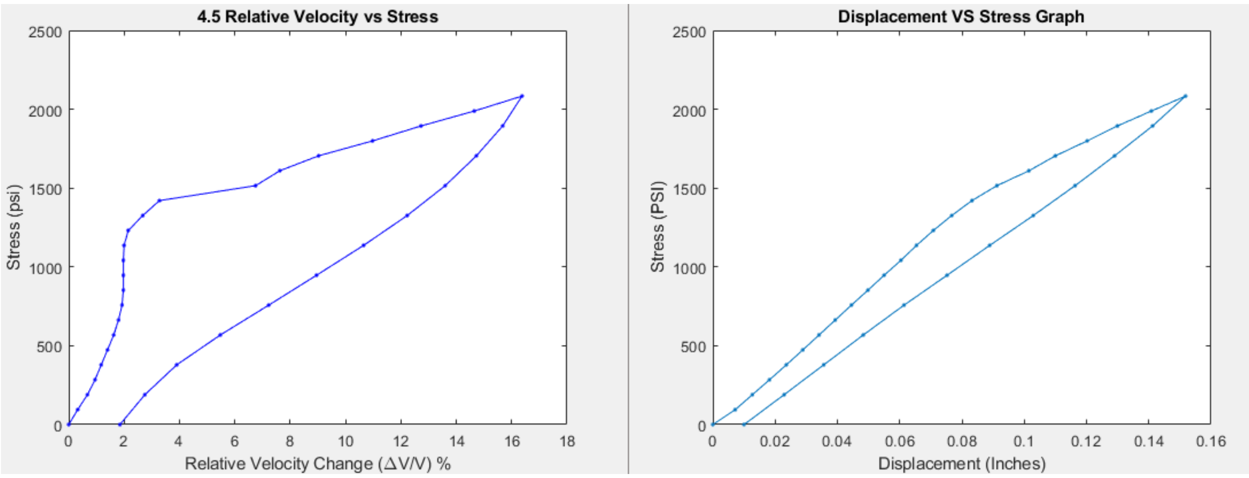

Figure 24 Small-scale PT Beam, 3-Point Load, Coda-wave Interferometry Test 4.5 - Graph of Relative Velocity vs. Stress and Displacement vs. Stress

5.2. Diffuse Ultrasound

The outcome being sought for diffuse ultrasound evaluation for the NDE of PT flexible filler systems is an indirect evaluation of the health of the post-tensioning system. For DU, this means having damaged feature recognition from increases in microcracking. This feature can indicate increased loading on the structure in question or a decrease in the effectiveness of the post-tensioned reinforcement allowing for more tension in the concrete.

5.2.1. Block Testing

The beam block specimens' testing will show the general feasibility and efficacy of the DU testing setup for identifying damage features relevant to flexible filler PT systems. These features would be identified via the coefficient of diffusivity plots generated by the DU algorithm. They would take the form of decreases in the diffusivity of the material due to an increase in the size or quantity of microcracking.

1. Test 1.3

The beam-block test serves the same purpose as it did with the CWI testing, to validate the effectiveness of this method and the equipment setup used to carry out testing. It was expected for an increase in microcracking to occur as the concrete was damaged from the direct compression testing. This trend can be clearly seen in Figure 25 via the diffusivity vs. stress plot. The diffusivity coefficient of a material is expected to decrease due to an increase in microcracking size and presence. Due to the presence of this effect, it can be assumed that the testing setup derived for DU testing was appropriate. It can also be seen that as the loading was reduced in the second half of the loading cycle, the coefficient of diffusivity increased again but did not return to its prior level before loading; both of these effects were expected as the microcracking in the specimen receded with the unloading of the beam-block.

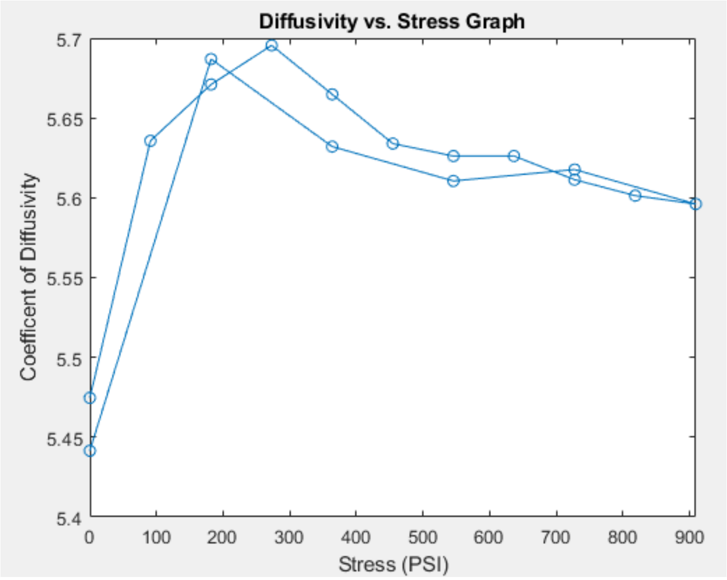

Figure 25 Small-scale Beam-block, Direct Compression, Diffuse Ultrasound Test 1.3 - Graph of Coefficient of Diffusivity vs. Stress

A plot of the integration values of the intervals is shown in Figure 26 for this test's zero load initial point. On this plot is the best fit line, which is used to find the diffusivity value for the specified load point. The value for diffusivity is the coefficient D in Equation 2. The value D affects the slope of the decaying leg of the logarithmic function. As the value of diffusivity increases, the slope of the decaying leg of the logarithmic function increases. Therefore, as there is an increase in damage to the concrete, the general slope of the interval integration plot for a specific load point will also increase.

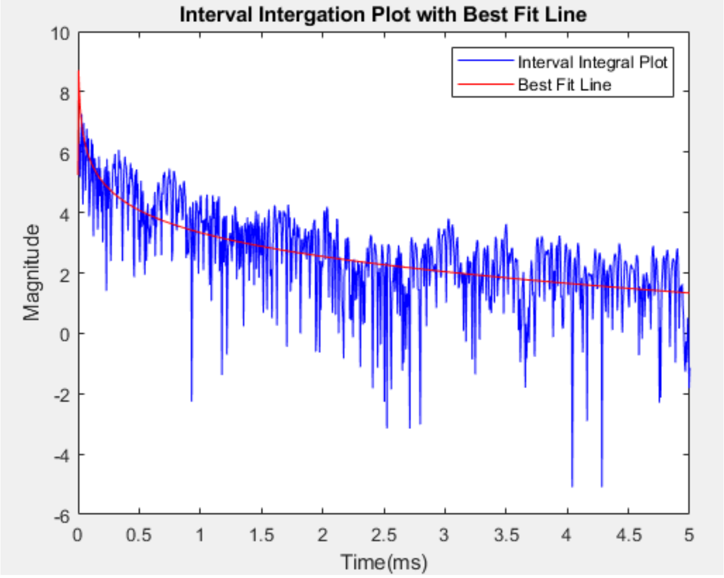

Figure 26 Interval Integration Plot with Best Fit Curve for Diffuse Ultrasound Spectroscopy

5.2.2. Beam Testing

After validating the testing setup with the beam block testing, the next step is small-scale beam testing in both normally reinforced and PT beams. These beams will undergo 3-point load testing, described in Chapter 4. In these tests, the same damage features as the beam-blocks. Drastic increases in microcracking presence could indicate deterioration of the PT system in full-scale structures.

5.2.2.1. Normally Reinforced

1. Test 2.2

Due to unknown circumstances in the testing process for the normally reinforced specimen, the data collected during the loading cycle could not provide any meaningful insight into the effectiveness of the DU method. The data points received followed no trends and seemed to randomly change slope and position without regard to the applied load. In future work, more testing on normally reinforced specimens would need to be done to identify the reasons behind the issues faced during these experiments. Due to time constraints, no further test could be completed after the defunct data for this specimen was discovered.

5.2.2.2. Post Tensioned

1. Test 4.2

Testing on the post-tensioned proved to be more fortunate than the normally reinforced beam. Test 4.2 was a loading and unloading cycle up to approximately 350 psi, resulting in no cracking of the specimen. Figure 27 shows the expected decrease in the coefficient of diffusivity that was also seen in Test 1.3. The presence of this trend in correlation to the displacement vs. stress plot shows that the decrease in the diffusivity coefficient occurred solely from the variation in microcracking caused by the loading cycle. The endpoint having a lower value of diffusivity than the starting point also proves the increase in microcracking in the structure from the load test.

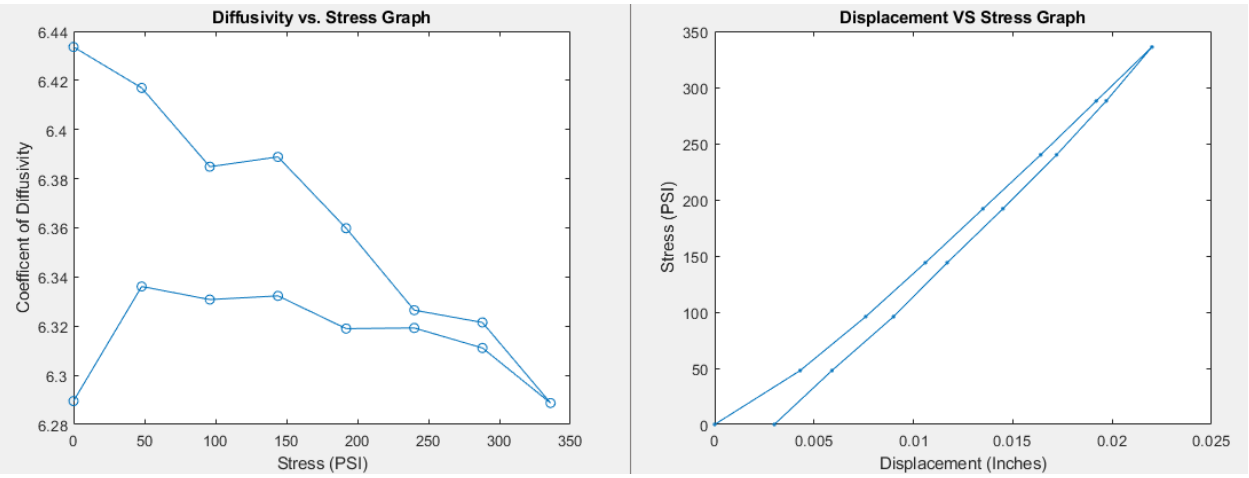

Figure 27 Small-scale PT Beam, 3-Point Load, Diffuse Ultrasound Test 4.2 - Graph of Coefficient of Diffusivity vs. Stress and Displacement vs. Stress

Chapter 6: Conclusions and Future Work

6.1 Future work

As previously stated, the planned full-scale testing could not be completed due to time constraints and extraneous circumstanced experience due to the COVID-19 pandemic. Since the methods tested during this research showed extremely promising small-scale results, it is highly recommended that work is continued in the future.

Large-scale testing would be the next logical step in the progression of this project. This testing would allow for a better application of the sensors to real-world scale concrete structures. The importance of this step would be to see how the sensors and equipment used to react to a much larger body of concrete and reinforcing steel, mainly to see if more powerful transducers are needed to excite the larger mass of concrete to receive signals that are representative of the entire body of the specimen. The large-scale specimens would also allow for a larger range of PT forces and applied loads which would gauge the sensitivity of both CWI and DU.

After large-scale testing is performed to fine-tune the equipment used for data collection, a better method of quantifying the data received would need to be researched and implemented. A preliminary recommendation would be to implement a self-learning algorithm trained with an initial dataset with desired input and output data specified. This algorithm would ideally be able to output basic outputs to direct more invasive evaluation techniques. These outputs could take the form of simple text stating, ‘Damage Likely’ or ‘Damage Unlikely’ or could go as far as identifying major and minor cracking or expected PT system failure.

A more unrealistic recommendation would be to implement constant monitoring on structures with flexible filler PT systems. This continuous monitoring would provide a much larger dataset for the self-learning algorithm and produce more accurate and specific results tailored to the structure type in which the PT system is implemented.

Implementing these recommendations for CWI and DU would provide a robust system for identifying PT system health in structures that implement post-tensioning with flexible fillers.

6.2 Conclusion

In this study, varying methods of NDE evaluation of flexible filler post-tensioned systems have been explored. Due to their effectiveness in evaluating concrete damage features, diffuse ultrasound and coda-wave interferometry were chosen for further research and experimental testing. This experimental testing consisted of normally reinforced concrete and post-tensioned concrete undergoing compression and 3-point load testing

Diffuse ultrasound was an effective method of indirectly evaluating the health of post-tensioned systems with flexible fillers. From the experimental testing, completed trends of the diffusivity coefficient were found to follow the previous research and decrease with an increase in microcracking severity.

Traditionally, constant monitoring would have to be done to compare how the diffusivity progressed with time and loading variations. However, it would be possible to implement this method into the routine biannual inspection performed by the FDOT on structures. By their nature, post-tensioned structures are large in size; multiple measurements could be taken and compared over varying areas of the structure. The measurements could be compared against one another to determine the relative health of certain PT strands via the value of diffusivity acquired from the tests. If the values are divergent enough during testing, further, more destructive testing could be ordered to evaluate the structure. Though this testing was generally successful, testing on the small-scale normally reinforced beam provided defunct results for no understandable reason; therefore, more testing into diffuse ultrasound is highly encouraged before implementing this method. Primarily, large-scale testing would tell how this method could be realistically implemented in routine inspections.

Coda-wave interferometry proved to be the most effective method for evaluating the condition of flexible filler post-tensioned systems tested in this study. The experimental testing showed that CWI could identify multiple signal features, including cracking, yielding, tensioning force, and mobilization of post-tensioned reinforcement. These results were most impressive when compared to traditional deflection testing. The results of CWI, relative velocity change plots, were significantly more sensitive to changes in the structure. Small shifts in the deflection plots were correlated to large and easily identifiable changes in relative velocity change plots.

As with diffuse ultrasound, CWI is traditionally observed as a monitoring type of NDE where constant measurements are taken to be compared against one another. Like DU, CWI measurements can be taken at multiple places on a post-tensioned structure and then compared to one another to allow for comparative analysis of how specific PT elements on a structure are behaving. If the plots are divergent enough during testing, further, more destructive testing could be ordered to evaluate the structure. It would be recommended that large-scale testing be performed on CWI before implementing this method.

Both methods explored in this paper are highly promising for evaluating post-tensioned systems using flexible fillers. Further research into the implementation of these methods is highly recommended due to their outstanding performance in small-scale testing.

Chapter 7: References

Ahn, E., Myoungsu, S., Popovics, J., & Weaver, R. (2019). Effectiveness of diffuse ultrasound for evaluation of micro-cracking damage. *Cement and Concrete Research*, 124. doi:https://doi.org/10.1016/j.cemconres.2019.105862

Anugonda, P., Wiehn, J., & Turner, J. (2001). Diffusion of Ultrasound in Concrete. *Ultrasonics*, 429-435. doi:S0041-624X(01)00077-4

Azizinanmini, A. (2012). *Improved Inspection Techniques for Steel Prestressing/Post-Tensioning Strand.* Miami: FDOT.

Chase, S. (2020). *Magnetic Flux Leakage Device for Evaluation of Prestressed Concrete Box Bridges.* Charlottesville: VDOT.

Deroo, F., Kim, J., Qu, J., Sabra, K., & Jacobs, L. (2010). Detection of damage in concrete using diffuse ultrasound (L). *Journal of the Acoustical Society of America*, 127. doi:10.1121/1.3409480

FDOT. (2016). *Structures Design Guidelines.* Tallahassee: FDOT.

FDOT. (2021). *Structures Design Guidelines.* Tallahassee: FDOT.

Fernandes, B., & Nims, D. (2014). Comprehensive MMF–MFL inspection for corrosion detection and estimation in embedded prestressing strands. *Journal of Civil Structural Health Monitoring*, 43-55. doi:10.1007/s13349-013-0061-4

Gondim, R., & Haach, V. (2021). Monitoring of ultrasonic velocity in concrete specimens during compressive loading-unloading cycles. *Construction and Building Materials*, 302. doi:10.1016/j.conbuildmat.2021.124218

Hurlebaus, S., Hueste, M. B., Karthik, M., & Terzioglu, T. (2016). *Condition assessment of bridge post-tensioning and stay cable systems using nde methods.* College Station: NCHRP.

Larose, E., & Hall, S. (2009). Monitoring stress related velocity variation in concrete with a 2*10^−5 relative resolution using diffuse ultrasound (L). *Journal of the Acoustical Society of America*, 1853-1856. doi:10.1121/1.3079771

Larose, E., Rosny, J., Margenrin, L., Anache, D., Gourdard, P., Campillo, M., & Tiggelen, B. (2006). Observation of multiple scattering of kHz vibrations in a concrete structure and application to monitoring weak changes. *Physical Review*, 73. doi:10.1103/physreve.73.016609

Planes, T., & Larose, E. (2013). A review of ultrasonic Coda Wave Interferometry in concrete. *Cement and Concrete Research*, 248-255. doi:10.1016/j.cemconres.2013.07.009

Quiviger, A., Payan, C., Chaix, J., Garnier, V., & Salin, J. (2011). Effect of the presence and size of a real macro-crack on diffuse. *NDT&E International*, 128-132. doi:10.1016/j.ndteint.2011.09.010

Stahler, S., & Sens-Schonfelder, C. (2011). Monitoring stress changes in a concrete bridge with coda wave interferometry. *Journal of the Acoustical Society of America*, 1945-1952. doi:10.1121/1.3553226

Uchino, K. (2017). *Advanced Piezoelectric Materials.* Woodhead Publishing in Materials. doi:https://doi.org/10.1016/B978-0-08-102135-4.00001-1

Xu, F., Wang, X., & Wu, H. (2012). Inspection method of cable-stayed bridge using magnetic flux leakage detection: principle, sensor design, and signal processing. *Journal of Mechanical Science and Technology*, 661-669. doi:10.1007/s12206-011-1234-x

Zhang, Y., Abraham, O., Grondin, F., Loukili, A., Tournat, V., Duff, A., . . . Durand, O. (2012). Study of stress-induced velocity variation in concrete under direct tensile force and monitoring of the damage level by using thermally-compensated Coda Wave Interferometry. *Ultrasonics*, 1038-1045. doi:10.1016/j.ultras.2012.08.011